The Internal Cranial Anatomy of the Middle Pleistocene Broken Hill 1 Cranium

Antoine Balzeau, Laura T Buck, Lou Albessard, Gaël Becam, Dominique Grimaud-Hervé, Todd C Rae, Chris B Stringer

The Internal Cranial Anatomy of the Middle Pleistocene Broken Hill 1 Cranium

ANTOINE BALZEAU
Équipe de Paléontologie Humaine, UMR 7194 du CNRS, Département Homme et Environnement, Muséum national d'Histoire naturelle, Paris, FRANCE; and, Department of African Zoology, Royal Museum for Central Africa, B-3080 Tervuren, BELGIUM; abalzeau@mnhn.fr

LAURA T. BUCK
Earth Sciences Department, Natural History Museum, Cromwell Road, London SW7 5BD; Division of Biological Anthropology, University of Cambridge, Pembroke Street, Cambridge CB2 3QG; and, Centre for Evolutionary, Social and InterDisciplinary Anthropology, University of Roehampton, Holybourne Avenue, London SW15 4JD, UNITED KINGDOM; lb396@cam.ac.uk

LOU ALBESSARD
Équipe de Paléontologie Humaine, UMR 7194 du CNRS, Département Homme et Environnement, Muséum national d'Histoire naturelle, Paris, FRANCE; lou.albessard@mnhn.fr

GAËL BECAM
Équipe de Paléontologie Humaine, UMR 7194 du CNRS, Département Homme et Environnement, Muséum national d'Histoire naturelle, Paris, FRANCE; gael.becam@cerotautavel.com

DOMINIQUE GRIMAUD-HERVÉ
Équipe de Paléontologie Humaine, UMR 7194 du CNRS, Département Homme et Environnement, Muséum national d'Histoire naturelle, Paris, FRANCE; dgherve@mnhn.fr

TODD C. RAE
Centre for Evolutionary, Social and InterDisciplinary Anthropology, University of Roehampton, Holybourne Avenue, London SW15 4JD, UNITED KINGDOM; t.rae@roehampton.ac.uk

CHRIS B. STRINGER
Earth Sciences Department, Natural History Museum, Cromwell Road, London SW7 5BD, UNITED KINGDOM; c.stringer@nhm.ac.uk

submitted: 20 December 2016; accepted 12 August 2017

ABSTRACT

The cranium (Broken Hill 1 or BH1) from the site previously known as Broken Hill, Northern Rhodesia (now Kabwe, Zambia) is one of the best preserved hominin fossils from the mid-Pleistocene. Its distinctive combination of anatomical features, however, makes its taxonomic attribution ambiguous. High resolution microCT, which has not previously been employed for gross morphological studies of this important specimen, allows a precise description of the internal anatomical features of BH1, including the distribution of cranial vault thickness and its internal composition, paranasal pneumatization, pneumatization of the temporal bone and endocranial anatomy. Relative to other chronologically and taxonomically relevant specimens, BH1 shows unusually marked paranasal pneumatization and a fairly thick cranial vault. For many of the features analyzed, this fossil does not exhibit the apomorphic conditions observed in either Neandertals or *Homo sapiens*. Its morphology and the general shape of the brain and of the skull may be partly explained by an allometric relationship relative to the features observed in *Homo erectus s.l.* However, further research is still necessary to better appreciate the cranial anatomy of BH1 and the role of *Homo rhodesiensis*/*Homo heidelbergensis* in the course of human evolution.

This paper also deals with more general aspects of scientific practices in paleoanthropology. In particular, we give precise descriptions of many internal anatomical features of Broken Hill 1, a specimen discovered in 1921. This important and unique dataset will allow independent comparative studies in the future. However, we were limited in our study by the very restricted amount of comparative information available for *Homo* fossils. In our view, scientific papers dealing with the anatomical description of hominin specimens, both in the case of announcements of new discoveries and of discussions of important specimens found decades ago, should always include qualitative and quantitative data that truly allow for further independent research.

  ISSN 1545-0031
doi:10.4207/PA.2017.ART107

Figure 1. BH1 cranium. Left to right: norma frontalis, norma lateralis *left,* norma occipitalis *(© The Trustees of the Natural History Museum, London).*

INTRODUCTION

The cranium from Broken Hill (BH1, Figure 1) is a key specimen in the study of human evolution as it is one of the best preserved fossils from the mid-Pleistocene. This time period corresponds to an increase in morphological variability (and possibly in specific diversity) in the hominin fossil record and the unusual combination of anatomical features in BH1 makes its taxonomic attribution ambiguous (e.g., Rightmire 2013, 2017; Stringer 2012a; Stringer and Buck 2014; Wood 2011). We present here a detailed description of its exo-, endo-, and intracranial features in order to: 1) clarify the anatomy of the specimen relative to existing knowledge of cranial evolution and variation in the mid-Pleistocene; and, 2) contribute to discussion about access to, and dissemination of, scientific data concerning our common human heritage and future perspectives in paleoanthropology.

BH1 was discovered by lead miners in 1921 in a quarry at Broken Hill, Northern Rhodesia (now Kabwe, Zambia) (Schwartz and Tattersall 2002; Wood 2011; Woodward 1921). The site was apparently named for the shape of the hill, which is marked by a depression, and because it resembled a mine in Australia of the same name (Wood 2011). In 1921–1925, further fossil human remains (all postcrania, with the exception of a small cranial fragment and a single maxilla [see Buck and Stringer 2015]) representing at least two additional individuals were found (Schwartz and Tattersall 2002); extinct fauna and Middle Stone Age lithics also were recovered from the same site (Wood 2011). BH1 has been dated to approximately 700–300 ka, mainly using faunal correlations with other middle Pleistocene sites in southern and eastern Africa (Klein 2009; Millard 2008). New ESR and U-series dating, however, is currently underway; preliminary results suggest that the cranium is younger, dating to approximately 250–300 ka (Buck and Stringer 2015; Stringer 2013).

Upon its discovery, BH1 initially was designated as the holotype for the new species, *Homo rhodesiensis* (Woodward 1921). Pycraft (1928) then mistakenly reconstructed a stooping posture from the Broken Hill postcrania (Schwartz and Tattersall 2002) and used this to propose a new genus—'*Cyphanthropus*.' Fortunately, this taxonomic error mostly was ignored and the specimen's *H. erectus*, *H. sapiens*, or supposed Neandertal[1] affinities alternately were highlighted over the next few decades (Oakley et al. 1977). Recently, BH1 often has been included in *H. heidelbergensis*, where it has formed an important part of the Euro-African hypodigm for this taxon for many researchers (e.g., Rightmire 2013; Stringer 2012a; Stringer and Buck 2014; Wood 2011), due to its similarities to other mid-Pleistocene fossils, particularly Petralona from Greece.

The external morphology of BH1 has been described previously (beginning with Pycraft 1928), and its robusticity, the thickness of its cranial vault (Balzeau 2013) and its extensive paranasal pneumatization (e.g., Seidler et al. 1997) have been remarked upon, but many aspects of the anatomy of the specimen remain poorly documented and require quantitative analysis in the context of the current knowledge of other fossil hominins. Here, high resolution microCT is employed to describe and quantify the internal morphology (vault thickness, dental root morphology, paranasal and temporal pneumatization, endocast morphology, and internal paleopathology) of BH1 in detail for the first time.

Cranial vault thickness (CVT) is a feature that is frequently discussed in analyses of fossil hominin specimens (Hublin 1978; Le Gros Clark 1964; Stringer 1984; Weidenreich 1943; Wood 1984), yet previous studies (Antón 1997; Balzeau 2006, 2007, 2013; Bräuer 1990; Bräuer and Mbua 1992; Brown 1994; Gauld 1996; Kennedy 1991; Kennedy et al. 1991; Pope 1992) have obtained dissimilar results and reached conflicting interpretations of this feature. This variation notwithstanding, CVT has often been used for taxonomic attribution of hominin specimens, including BH1 (e.g., Baba et al. 2003; Curnoe and Green 2013; Delson et al. 2001; Grimaud-Hervé et al. 2012; Indriati and Antón 2010; Kappelman et al. 2008; Kennedy et al. 1991; Manzi et al. 2003; Potts et al. 2004; Rosas et al. 2008). CVT is awkward to

quantify and compare directly between specimens because various methodological limitations make its precise and replicable quantification difficult, even when using modern slice-based imaging methodologies (see Balzeau 2006, 2007, 2013). When this feature has been quantified in the past, generally only one or very few measurements with questionable anatomical homology and reproducibility were compared. Here, we quantify the CVT of BH1 in a detailed and replicable way using microCT data, in order both to characterize its expression in this fossil and to enable better future comparisons with other specimens.

Recent study of CVT (Balzeau 2013) has strengthened the view that "caution should be exercised in treating absolute values of cranial bone thickness as diagnostic phylogenetic traits" (Gauld 1996, p. 420). Indeed, a more detailed examination of the frontal squama and parietals in the parasagittal area (Balzeau 2013) cast serious doubt on the long-standing interpretation that *H. erectus* displays an autapomorphically thicker cranial vault than other hominins. There are some general differences, however, between hominin species in the distribution of bone thickness along the parasagittal region of the upper vault; Neandertals and *H. sapiens* show two distinct apomorphic conditions (Balzeau 2013). New comparative descriptive and quantitative data, including more detailed information from other areas of the vault, such as that presented here for BH1, are necessary to better understand variation in and patterns of CVT in hominins. Furthermore, we analyze the relative position of inion and endinion and the relationships between the exo- and endocranial structural features of the occipital bone (Balzeau et al. 2011) in BH1 compared with other hominin specimens. These measurements characterize important shape characteristics of the occipital bone, which is crucial to the study of hominin evolution because it has several features that help to differentiate between various hominin species (Balzeau et al. 2011). In addition, our study provides additional data to analyze and understand cranial features and their related internal variations, which have been suggested to be diagnostic of the taxonomically much disputed "mid-Pleistocene assemblage" (Rightmire 2001; 2004, 2013).

The internal structure of teeth is also a matter of interest to document hominin evolution, with differences in morphology reported to differentiate between closely related species (e.g., Smith et al. 2012). We focus here on the tooth roots because of the many carious lesions that have affected the crowns of BH1 (Lacy 2014), obscuring their morphology, and because this anatomical area has recently been shown to vary between hominin species (Le Cabec et al. 2013) and also between other primate taxa (Moore et al. 2013, 2015).

Variation in hominin craniofacial pneumatization is another aspect of internal cranial anatomy that is still incompletely understood, despite a long history of study (e.g., Buck 2014; Buck et al. 2012; Busk 1861; Blake 1864; Rae et al. 2011; Tillier 1975, 1977; Zollikofer et al. 2008). Nevertheless, the presence and size of paranasal sinuses has been used in the systematic evaluation of several species (Farke 2010; Rae 1999) and large sinuses have been proposed as a diagnostic trait of *H. heidelbergensis* (Prossinger et al. 2003; Seidler et al. 1997; Stringer 2013). As the alpha taxonomy of mid-Pleistocene hominins has been disputed for many years (e.g., Buck and Stringer 2014; Harvati 2007; Manzi 2016; Mounier 2009; Mounier et al. 2009; Rightmire 1996, 1998, 2008, 2013, 2017; Stringer 1983, 1985, 2012a, 2012b), any morphological trait, such as distinctive paranasal pneumatization, that distinguishes between species is potentially important. Since most mid-Pleistocene hominin material is craniodental, their alpha taxonomy is best established on the basis of craniofacial or dental characters. Therefore, investigating the size and level of variation in the pneumatization of these specimens, including BH1, can potentially clarify their taxonomy.

Temporal pneumatization is also taxonomically variable within the tribe Hominini. The primitive condition is represented by the extant non-human great apes, with extensive pneumatization throughout the entire temporal bone. Contrary to previous suggestions, specimens attributed to *Australopithecus africanus* and *Paranthropus* do not share the ape-like pattern of pneumatization and show a reduction in the degree of cell expansion (Balzeau 2015). *H. erectus* individuals from Zhoukoudian and possibly the fossils from Dmanisi as illustrated by D 22800 (de Lumley et al. 2006; Rightmire et al. 2006) have a somewhat reduced, but still extensive, propagation of pneumatization with inter-individual variation. Other early *Homo*, *H. erectus* individuals from Ngandong and Sambungmacan, Neandertals, and *H. sapiens* have a still more restricted distribution of pneumatization, but its level in mid-Pleistocene *Homo* specimens, such as BH1, is largely uncharacterized. Although temporal bone pneumatization shows some individual variability, a similar pattern of distribution was found in all adult Neandertal individuals from Krapina and western Europe, in which pneumatization is mainly restricted to most parts of the petromastoid areas (Balzeau and Radovčić 2008). Neandertals are unique in this configuration and particularly in its intraspecific homogeneity. Conversely, temporal bone pneumatization varies greatly in recent *H. sapiens*. It is generally limited to the mastoid, perilabyrinthine, and petrous regions, while propagation into the squamous temporal is rare and not extensive (e.g., Allam 1969; Bronoosh et al. 2014; Hill 2008, 2011; Hill and Richtsmeier 2008; Schulter 1976, Scheuer and Black 2000; Schulter-Ellis 1979; Virapongse et al. 1985; Wolfowitz 1974; Zonneveld 1987). Correlations between the shape of the pneumatization and the shape of the temporal bone also illustrate some particularities (Balzeau and Grimaud-Hervé 2006), but this field of research also requires further analyses. Our detailed characterization of the temporal pneumatisation of BH1 will contribute to the emerging picture of its expression in the genus *Homo* and will facilitate consideration of the morphological and environmental correlates of pneumatization in hominins.

Finally, paleoneurology is an important field in the study of hominid evolution and hominin diversity. Variation in the size and shape of the endocranium may differ-

entiate fossil hominin species; for example, Asian *H. erectus* specimens are differentiated from all other samples of the genus *Homo*, including the African and Georgian specimens that are also often included in *H. erectus* (Grimaud-Hervé and Lordkipanidze 2010), by significantly smaller relative parietal and temporal lobes compared with other groups (Balzeau et al. 2012). Neandertals and *H. sapiens*, in addition to sharing some of the largest endocranial volumes of all hominins, show different relative contribution of the frontal, parieto-temporal, and occipital lobes (Balzeau et al. 2012; Grimaud-Hervé 1997). Completing a detailed study of the endocast of BH1 is important because this specimen is encephalized compared to its probable predecessors—one of the traits that could characterize a potential last common ancestor of Neandertals and *H. sapiens*.

The study of these informative internal cranial traits is facilitated by high resolution microCT, which has not previously been employed on this important specimen. The complete description of the internal features of BH1 as detailed here is crucial to fully understand the anatomy of the specimen. It will also be useful for future studies by all researchers. Following the description, comparisons are made with data on these anatomical features in other chronologically and geographically relevant specimens. Finally, we try to interpret the available information to understand the anatomical characteristics of BH1 and modalities of evolution of mid-Pleistocene hominins.

One dramatic limitation to this study has been access to appropriate comparative samples, as the anatomy of most of the features studied here has not yet been described for the majority of the most emblematic specimens of the mid-Pleistocene. Instead of conducting several separate analyses for each feature on restricted and unsatisfactory samples, we decided to focus here on the anatomy of the cranium of Broken Hill 1. We also provide a complete landmark description of the skull (in Supplementary Information–SI1[2]). The information detailed here will be useful for future research, by us and others, and we hope that this work will stimulate similarly exhaustive descriptions of other important fossil hominin specimens.

MATERIAL

BH1 is largely complete (see Figure 1), missing only the right temporal bone, part of the occipital bone, the cranial base on the right side and the area of the external occipital protuberance. The missing bone corresponds endocranially to the right cerebellar and temporal lobes as well as to most of the right occipital lobes. The preservation of the cranial surfaces, including the exo- and endocranial surfaces, and of the internal structures, is exceptional in a fossil of this age. The maxilla of BH1 includes 15 teeth, including 2 central incisors, 1 lateral incisor (left), 2 canines, 4 premolars, and 6 molars. Some lesions are visible and will be described below. Because anatomical description of the external aspects of the specimen is already available elsewhere (Pycraft 1928; Rightmire 2017; Schwartz and Tattersall 2003), the focus of the present contribution is instead on original information enabled by the internal imaging data. The endocranial cast has already been partly described (Elliot Smith 1928); this description is completed here and comparisons are made with other fossil hominin endocasts, material that was scarce at the time of the original description.

MICROCT DATA

The BH1 fossil was scanned by one of us (LTB) on a Metris X-Tek HMX ST 225 microCT scanner at the Natural History Museum, London, with the following parameters: voltage: 210 KV, current: 175 µA, filter: 6mm Cu, exposure: 1415 ms. The resulting data were reconstructed using CT-PRO software version 2.0 (Metris X-Tek, Santa Clara).

The specimen is highly mineralized, but this has not caused any substantial imaging artifacts; there are no overflow artifacts and, although some noise is present, this has only limited influence. Therefore, the main limitations of the data are due to the spatial resolution of the data (due to the size of the specimen and the limited field of view available in the microCT scanner) and to the partial volume averaging artifact, which is inherent to CT methodologies (Balzeau et al. 2010). The resolution of the microCT dataset is 0.127mm^3, the resulting error is therefore around ±0.065mm.

COMPARATIVE SAMPLES

The BH1 fossil is compared to the material used in recent studies of internal cranial features in fossil hominins and hominids. For CVT, comparison is possible (Balzeau 2006, 2007, 2013; Balzeau and Charlier 2016) with a total of 125 adult specimens, including 27 hominins from several species (Sts 5, KNM-ER 1813, 3733, 3883, Tighennif 4, Sangiran 2, 4, 17, Ngandong 1, 7, 12, Ngawi 1, Sambungmacan 1, 3, Liang Bua 1, La Chapelle-aux-Saints 1, La Ferrassie 1, Guattari 1, Krapina, 3, 4, 5, 6, La Quina H5, Saccopastore 1, Spy 1, Spy 10, Petralona), 23 fossil anatomically modern humans (labelled fossil AMH below; Cro-Magnon 1, 2, 3, Mladeč 1, Pataud 1, skulls from African Epipaleolithic sites of Afalou Bou Rhummel [6] and Taforalt [6], the Upper Paleolithic skull from Rochereil, the skull from Song Terus dated between 5700 and 9400 BP, and three skulls from the Mesolithic site of Téviec), 40 recent European *H. sapiens* (labelled recent AMH below), and 35 *Pan paniscus*.

For comparisons of paranasal pneumatization, two important and relatively complete mid-Pleistocene (putative *H. heidelbergensis*) specimens were used—Bodo (Ethiopia) and Petralona (Greece). The fossil cranium from Petralona was found in Petralona Cave, near Thessaloniki, Greece in 1959. Due to a lack of preserved *in situ* sediments, it has been difficult to date; based on fauna from the cave, the cranium is thought to be approximately 350–730 ka, but there is considerable debate over whether the fauna and the hominin fossil are associated, and the hominin cranium may be nearer the lower value, possibly about 400 ka (Stringer 1983). However, electron spin resonance analysis of a flowstone thought to have bracketed the cranium suggests a much younger date of 150–200 ka (Grün 1996). The Bodo cranium was found in the Middle Awash Valley of Ethiopia in 1976. It is currently dated to approximately 600

ka using chronostratigraphic methods (Clark et al. 1994).

Information on temporal bone pneumatization variations in recent *H. sapiens* was taken from the literature (e.g., Allam 1969; Bronoosh et al. 2014; Hill 2008, 2011; Hill and Richtsmeier 2008; Scheuer and Black 2000; Schulter 1976; Schulter-Ellis 1979; Virapongse et al. 1985; Wolfowitz 1974; Zonneveld 1987) and from our own publications on the topic, which also address the morphology of this feature in Neandertals, Asian *H. erectus*, and African hominins (Balzeau 2015; Balzeau and Grimaud-Hervé 2006; Balzeau and Radovčić 2008).

A morphometric comparison of endocranial anatomy is performed with large samples of fossil hominins (KNM-ER 1470, 1813, 3733, 3883, KNM-WT 15000, LH 18, Salé, Dmanisi 2280, 2282, Trinil 2, Sangiran 2, 10, 17, '*Sinanthropus*' III, X, XI, XII, Erhingsdorf H9, Reilingen, Spy 1, 10, Teshik-Tash, La Chapelle aux Saints, Le Moustier, La Quina H5, Feldhofer, Jebel Irhoud 1, 2) and anatomically modern humans (Predmostí 3, 4, 9, 10, Cro-Magnon 1, 3, Dolní Věstonice 1, 2, Pataud and 104 recent humans) (Balzeau et al. 2013; Grimaud-Hervé 1997; Grimaud-Hervé and Lordkipanidze 2010).

Finally, a combined study of the exocranial and endocranial variation along the mid-sagittal plane was carried out to analyze the position of the Broken Hill fossil relative to other *Homo* specimens, following a protocol described elsewhere (Albessard et al. 2016). A sample of 41 recent humans and several fossils of the genus *Homo* was selected according to the preservation state of the specimens. We analyzed data from Chinese and Indonesian *H. erectus* (Zhoukoudian III, X, XI, XII, Sangiran 2, Ngandong 7, 12, Ngawi, Sambungmacan 3), African *H. erectus* specimens (KNM-ER 3733, 3883), the mid-Pleistocene fossil from Petralona, and Neandertals (La Ferrassie 1, La Chapelle aux Saints 1, Guattari 1, Spy 1). The fossil *H. sapiens* sample comprises of Middle Paleolithic specimen Skhūl V, Upper Paleolithic specimens Cro-Magnon 1 and 3, Pataud 1, Lafaye 1, Cioclovina 1, Mueirii 1 and Mladeč 1, and Epipaleolithic/Mesolithic specimens from Afalou Bou Rhummel (12,34), Taforalt (XIc1), and Téviec (9, 16). We used two-dimensional images of cross-sections of the skull extracted from CT data for all extant and fossil *H. sapiens*, as well as for most of the fossil *Homo* sample. For the Zhoukoudian individuals, we used cross-sections drawn and published by Weidenreich (1943).

METHODS

Multiplanar reformatting, thresholding procedures, three-dimensional volume rendering, segmentation, 3D topographic mapping (with the module SurfaceDistance), measurement, and illustration acquisition were performed in Avizo 7 and 8 (FEI, Hillsboro, Oregon). Selection of regions of interest on the 3D models for CVT analysis was performed using Geomagic (3D Systems). Using the imaging datasets, the boundary between the bone and the surrounding air, or when necessary with the existing sedimentary matrix, was identified on each individual slice by manual segmentation. This procedure consists of measuring the median value (or half maximum height, HMH) from the CT value of the two elements, of which the interface should be defined (Spoor and Zonneveld 1993). This manual segmentation was done at multiple points along the bone surface of the vault with adapted settings to study CVT and the virtual endocast. This procedure allowed for accurate identification of the interface between two structures (Balzeau et al. 2010) and therefore the isolation of the exact area corresponding to the bone extent to quantify CVT. The same procedure was used to delimit the extension of the bone tables and of the diploë. Statistical procedures used to analyze the recorded data were conducted in PAST 3 software (Hammer et al. 2001). Statistical comparisons of individual values for bone thickness in BH1 and comparison with samples were performed with a specific individual's test score as described by Sokal and Rohlf (1995) and modified by Crawford and Howell (1998).

We quantified the 3D coordinates of a long list of landmarks (n=70) on the 3D model of the skull BH1 (in Supplementary Information–SI1) using Avizo (FEI, Hillsboro, Oregon). These landmarks characterize the face (n=32), the calvaria (n=19) and the endocranial surface (n=19).

VARIATIONS IN CVT AND STRUCTURAL BONE COMPOSITION

Imaging methodologies allow new possibilities (e.g., Balzeau et al. 2010; Spoor et al. 2000) for the study of CVT and its inter- and intra-individual variation, but many aspects have to be considered (Balzeau 2013) and various limitations make the precise and repetitive quantification of cranial vault thickness difficult when using slice-based technology. Here, three distinct protocols were developed to overcome the limitations of slice-based data are used to quantify CVT; these have been tested and validated elsewhere (Balzeau 2006, 2007, 2013).

1. The first quantifies CVT and structural composition of the cranial bones along the mid-sagittal plane. This plane is reproducible in different hominin species, as its definition is not influenced by variations in size and morphology of the different bones of the cranial vault. The mid-sagittal plane is the only CT slice perpendicular to the cranial thickness along its full extent. This methodological issue has not always been considered in previous studies of CVT, resulting in thickness measurements whose validity is questionable and that may be impossible to compare between specimens and studies (e.g., Curnoe and Brink 2010). CVT and structural bone composition are determined at 60 points along the mid-sagittal plane (Balzeau 2006, 2007; Figure 2). Between glabella and bregma, 20 values are measured. An additional 20 values are located between bregma and lambda, 15 between lambda and inion and 5 are taken along the nuchal plane. Bone thickness was not quantifiable on the complete mid-sagittal plane of BH1 because of the incomplete preservation of the specimen (see Figure 2); the external cranial surface is broken from the inferior third of the occipital plane to approximately the middle of the nu-

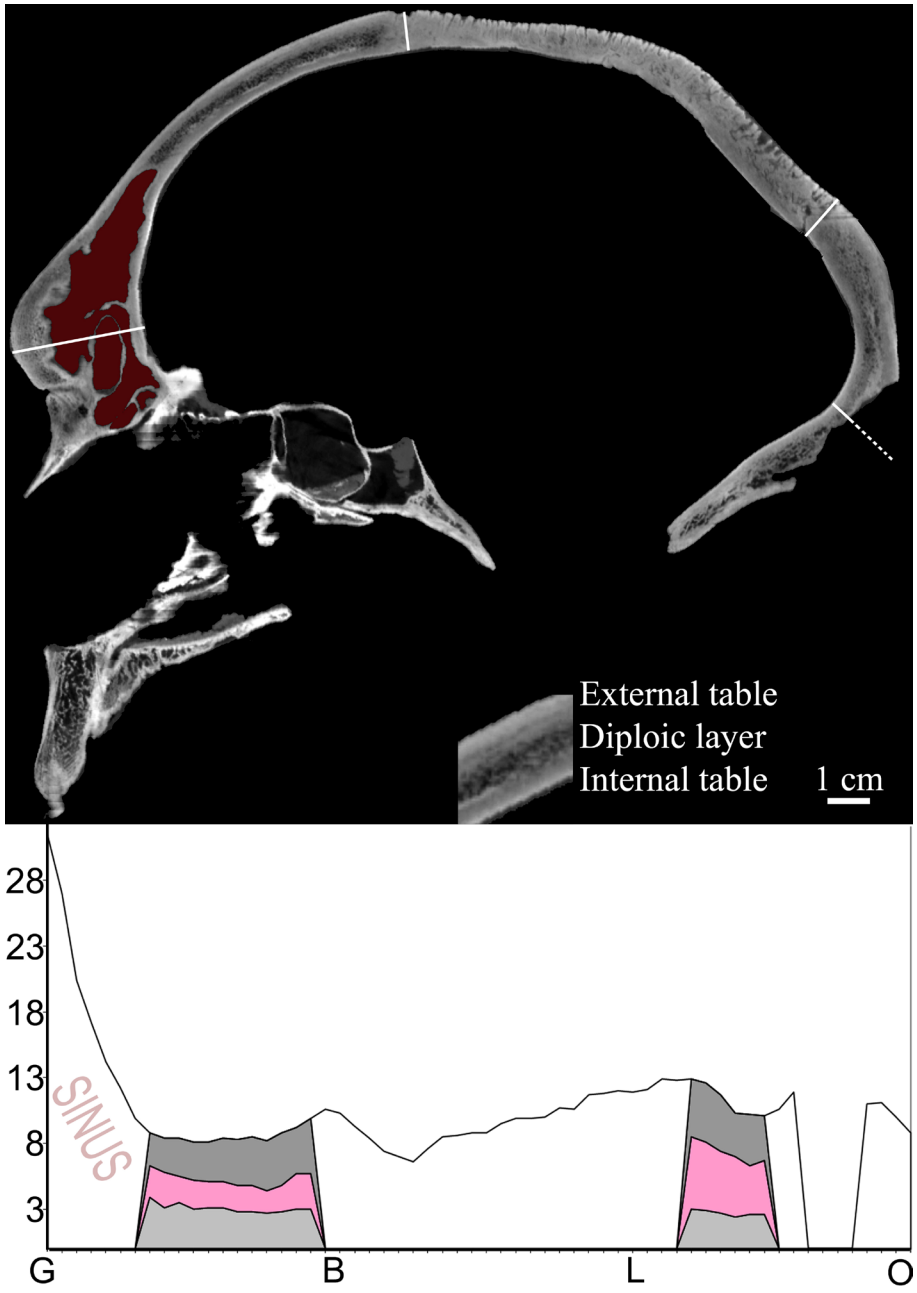

Figure 2. Illustration of the mid-sagittal plane for BH1 and variations in the thickness (in mm) of the cranial vault along the mid-sagittal plane. The cranial thickness is quantified from the glabella (G), through bregma (B), lambda (L) to the foramen magnum *(opisthion: O); the graphic representation of the data corresponds to the successive landmarks from left to right. Values for the thickness of the internal table (below), diploic layer and external table (above) are also given when measurable. The area labelled sinus corresponds to the extension of the frontal sinus; the breakage of the occipital superstructures led to incomplete documentation of the variation in bone thickness in this area.*

chal plane. As a result, the values for six points along the mid-sagittal plane are missing, including the value at the external occipital protuberance. Except for these points, CVT and bone composition were quantifiable on the rest of the mid-sagittal plane without being altered by post-mortem modifications of the specimen.

2. The second method uses computed maps of bone thickness variation to compare data over larger anatomical areas, instead of a series of measurements at precise locations (Balzeau 2013). From the 3D model of the skull, the exo- and endocranial surfaces were used to compute a 3D topographic map of the variation in total bone thickness (Figure 3). Bone thickness was calculated with the Surface Thickness module of the Avizo program. This tool computes the shortest distance of each vertex in the direction of its normal with all the triangles of the same material. In the case of the vault of BH1, over 900,000 thickness measure-

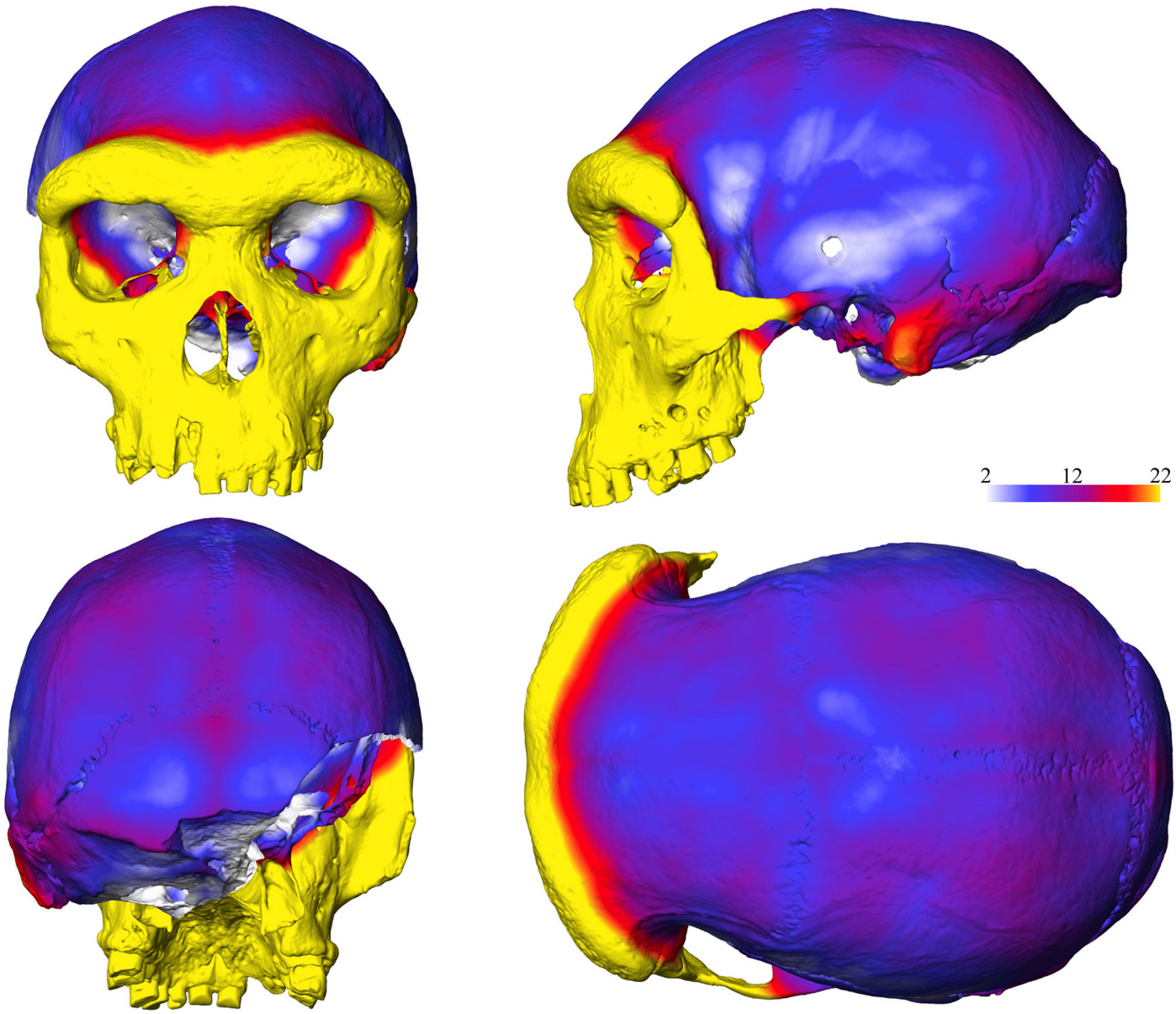

Figure 3. 3D topographic mapping of the variation of total bone thickness rendered using a color chromatic scale (thickness increasing from white to yellow, corresponding to a variation between 2mm and 22mm) in anterior, left lateral, posterior, and superior views.

ments were automatically quantified. These data were rendered using a chromatic scale, using a color scale between 2 and 22 millimetres from white to yellow. From the 3D topographic map, variations in CVT in selected areas were also extracted. Following the methodology of Copes (2012), mean thickness of the bone and its internal structure were quantified in a circular area 1.2cm in diameter in the center of the frontal bone, and in a similar area with a 2.5cm diameter in the centre of the parietal bone. These sizes were selected, based on the preservation of the bone and its orientation, to allow quantification of CVT only in well preserved areas, and to allow comparisons with variation for the areas reported for large recent human samples (Copes 2012; Marsh 2013).

3. Finally, CVT was quantified at classical anatomical landmarks. When calipers or a cephalometer are used directly on the original specimen, the value is an approximation on a small surface—due to the size of the surface of contact of the measuring tool—and for its orientation. Three dimensional imaging methodologies, as used here, however, allow a much higher precision, which results in thickness measurements that may vary by several millimetres within a few millimetres of one another. Thus, here, a mean value was obtained from multiple local quantifications, rather than a measurement from a single 3D point.

Using Avizo 7 (FEI, Hillsboro, Oregon), we quantified the relative position of inion and endinion, measured the distances between inion (denoted I), endinion (E), lambda

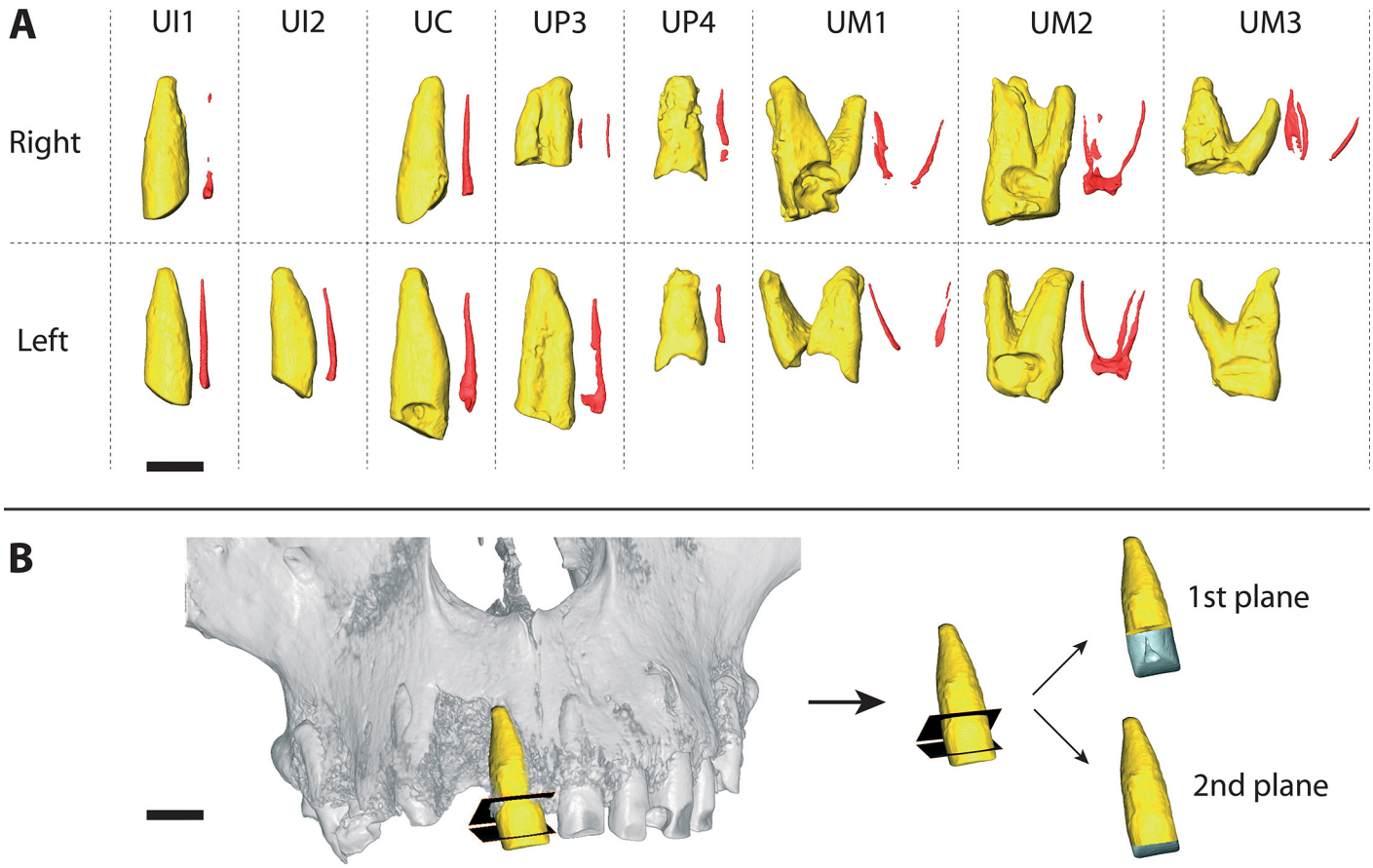

Figure 4. A) Three-dimensional reconstruction of the upper teeth of the Broken Hill 1 specimen (scale: 1cm). In yellow: the tooth; in red: the pulp cavity; UI1: upper central incisor; UI2: upper lateral incisor; UC: upper canine; UP3: upper third premolar; UP4: upper fourth premolar; UM1: upper first molar; UM2: upper second molar; UM3: upper third molar. B) Virtual cutting protocol with two planes for the upper central incisor (scale: 1cm).

(L), and opisthion (O), calculated the ratio between the exo- and endocranial distance of the squamous occipital and the nuchal plane (labelled LI/IO and LE/EO) and the exo- and endocranial proportions of the occipital bone as expressed by the L-inion cord (LIC), inion-opisthion cord (IOC), lambda-endinion cord (LEC), and endinion-opisthion cord (EOC). When scaled to endocranial volume, the distances were denoted with the suffix r.

DENTAL ROOT MORPHOLOGY

Each of the maxillary teeth was virtually extracted from its alveolus by using the Watershed tool in Avizo 7.1 to automatically segment out dental material based on thresholding. The selections automatically made by this tool were then corrected manually by using the Brush tool. The descriptions here concern only the tooth roots of BH1. We segmented out the pulp cavity for each of the teeth; however, we did not virtually separate out the enamel from the dentine, due to the voxel size of the microtomographic data (due to the imaging of the entire cranium) and the impregnation of the fossil by heavy metals during its burial in the lead mine at Broken Hill (Bartsiokas and Day 1993), which have changed the density of dental tissues. A comparative metric analysis is performed only for the anterior teeth (incisors and canines), given their greater simplicity and their lower degree of variation compared to the premolars and molars roots. The measurement protocol established by Le Cabec et al. (2013) consists of a virtual slice with an adjusted transverse plane through the lingual and labial sides of the cervical line to separate the root from the crown. However, in the absence of enamel to enable the location of the cervical line of BH1's central incisors, two virtual cutting planes were used to record the minimum and maximum lengths of the roots. The first plane takes into account the location of the tooth in the maxilla and follows the line of the alveoli. A second plane is determined taking into account the height of the cervical line of the left lateral incisor and the left canine, which retain their enamel (Figure 4B). For all the anterior teeth, linear measurements of the root dimensions were collected (root length: RL; mesiodistal and labiolingual root diameters: R(MD) and R(LL) in mm), along with surface area (root surface area of the labial and lingual parts: RSA lab and RSA ling) and volumetric parameters (root volume: RV; root pulp volume: RPV) (Table 1).

TABLE 1. LINEAR, SURFACE AREA, AND VOLUMETRIC PARAMETERS OF THE ANTERIOR TEETH OF BH 1.*

Specimen	Tooth	RL (mm)		R(MD) (mm)		R(LL) (mm)		RSA (mm²)		CA (mm²)		RV (mm³)		RPV (mm³)		R(MD)/R(LL) -	
BH1	URI1	*1st*	*2nd*	*1st*	*2nd*	*1st*	*2nd*	*1st*	*2nd*	*1st*	*2nd*	*1st*	*2nd*	*1st*	*2nd*	*1st*	*2nd*
		16.8	22.8	8.2	8.3	8.2	7.5	322.2	491.4	55.2	52.6	541.0	864.4	0.3	8.2	1.0	0.9
	ULI1	*1st*	*2nd*	*1st*	*2nd*	*1st*	*2nd*	*1st*	*2nd*	*1st*	*2nd*	*1st*	*2nd*	*1st*	*2nd*	*1st*	*2nd*
		17.4	22.0	7.9	8	8.6	8.6	329.4	463.4	56.6	47.3	530.6	784.5	11.5	21.3	1.1	1.1
	ULI2	19.1		6.2		8.0		369.0		43.2		567.3		13.8		1.3	
	ULC	24.6		7.4		10.0		540.1		59.9		914.2		31.2		1.4	

*1st: data from the first cutting plane; 2nd: data from the second cutting plane; RL: root length; R(MD): mesio-distal root diameter; R(LL): labio-lingual root diameter; RSA: root surface area; CA : cervical area; RV: root volume; RPV: root pulp volume; URI1: first right upper incisor; ULI1: first left lower incisor; ULI2: second left lower incisor; UJC : left upper canine.

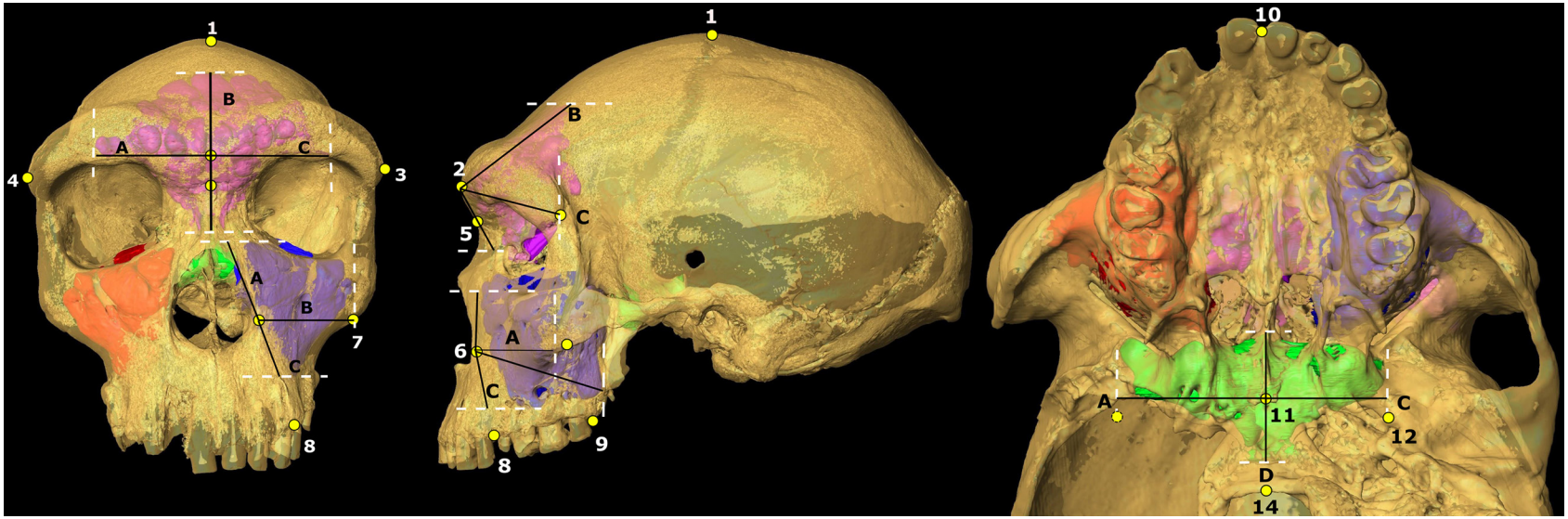

Figure 5. Extent measurements of BH1's sinuses as measured on 3D virtual reconstruction of microCT data rendered transparent with sinuses represented as colored solids (see Table 5). Craniometric landmarks indicated as yellow circles, numbered as in Table 2 (landmarks not visible in figured orientation are indicated with a dashed border). Frontal sinus (shown in magenta, figured on left hand [norma frontalis] *and middle* [norma lateralis] *diagrams): A) extent from glabella towards right frontomalare temporale; B) extent from glabella towards bregma; C) extent from glabella towards left frontomalare temporale; D) extent from glabella towards nasion. Left maxillary sinus (shown in blue, figured on left hand* [norma frontalis] *and middle* [norma lateralis] *diagrams): A) extent from left alare towards nasion; B) extent from left alare towards left zygomaxillare; C) extent from left alare towards left C/P3; D) extent from left alare towards left molars posterior. Sphenoidal sinus (shown in green, figured on right hand* [norma basilaris] *diagram): A) extent from hormion towards right foramen ovale posterior.; B) extent from hormion towards prosthion; C) extent from hormion towards left foramen ovale posterior; D) extent from hormion towards basion. Not to scale.*

TABLE 2. LANDMARKS USED IN SINUS EXTENT MEASUREMENTS (see Figure 5).

Landmark	Number
Bregma	1
Glabella	2
Left frontomalare temporal	3
Right frontomalare temporal	4
Nasion	5
Left alare	6
Left zygomaxillare	7
Left C/P3	8
Left molars posterior	9
Prosthion	10
Hormion	11
Left foramen ovale posterior	12
Right foramen ovale posterior	13
Basion	14

PNEUMATIZATION

Paranasal sinus size was measured in three ways: volume, surface area, and extent. Frontal, maxillary (left and right), and sphenoidal sinuses were manually segmented out slice-by-slice from the raw CT data in Avizo 8.0. The volumes and surface areas of these materials were then calculated using an Avizo automatic routine. A three-dimensional virtual reconstruction of the cranium was created and rendered transparent. The extent of the sinuses in BH1 in different directions was measured by placing craniometric landmarks (Figure 5 and Table 2) on the virtual reconstruction of the cranial surface and measuring from these landmarks to the greatest extent of the solid sinus material in the required direction using the Avizo 3D line measurement tool (see Figure 5). The ethmoid sinuses were not considered since their size, position and morphology make their measurement extremely difficult. This problem has prevented their inclusion in most previous work, resulting in almost no comparative literature for this sinus (e.g., Buck 2014; Tillier 1975, 1977; c.f. Zollikofer et al. 2008).

Sinus size in hominoids has been shown to scale with facial size (Holton et al. 2011; Koppe et al. 1999a, b; Lund 1988; Rae and Koppe, 2000; Rae et al. 2011; although see Butaric et al. 2010); thus, measures of sinus size standardized using a proxy for facial size also were examined when comparing sinus size in BH1 with that of other specimens. Following Rae et al. (2011) and Buck (2014), the distance from glabella to frontomalare temporale (G-FMT) was used to standardize measurements; this measurement has been shown to correlate strongly with more complex measures of facial size, such as centroid size (Buck 2014), but is less problematic when comparing samples of fragmentary specimens. G-FMT was squared to standardise areas and cubed to standardise volumes to preserve the same units of measurement.

ENDOCRANIAL ANATOMY

The endocranial surface of BH1 was studied on both a physical replica of the original specimen and on a virtual reconstruction produced from the microCT data.

Measurements of the endocast are given in Table 3. Measurements of the length, height, and width of different areas of the endocast were performed using sliding and spreading callipers on physical endocasts and on drawings for dimensions quantified in projection views of the endocast. The virtual models were quantified in Avizo. The frontal, parietal, and occipital chords were quantified based on anatomical landmarks related to brain structures. The surfaces of the frontal, parieto-temporal, occipital, and cerebellar lobes also were measured (Balzeau et al. 2013; Grimaud-Hervé 1997). These variables were selected because they refer to real variation in the shape of the brain and not to internal distances within the endocranium as often used (e.g., maximal dimensions of the intracranial cavity, distances from internal cranial landmarks such as endobregma, and others).

Various components of endocranial petalias (the antero-posterior, vertical, and lateral components of the protrusions of the frontal and occipital poles) (Balzeau and Gilissen 2010; Balzeau et al. 2012) were quantified, as well as the size, shape, and bilateral asymmetries of the third frontal convolution (or posterior inferior frontal gyrus) (Balzeau et al. 2014). The parameter FA11 quantifies the asymmetries for all individuals and all traits, and is calcu-

TABLE 3. DEFINITIONS OF ENDOCRANIAL MEASUREMENTS AND VALUES (in mm for all measurements except the surface data, which are in mm²) FOR BH1 (see Balzeau et al., 2103, 2014; Grimaud-Hervé et al. 2010 for complete definitions and illustrations).

Abbreviation	Definition	Measurement
MLE	Maximum length (PCA)	172
MWE	Maximum width (PCA)	137
WSE	Maximum width measured at the supramarginal gyri	123
WPfE	Maximum width measured at the foot of the 2nd parietal convolutions	125
WBcE	Maximum width measured at Broca's cap	101
WOfE	Maximum width measured at the orbital part of the 3rd frontal convolutions	78
WFfE	Maximum width measured at the foot of the 3rd frontal convolutions	108
BBHE	Endobasion-endobregma height	120
BVHE	Endobasion-endovertex height	119
MHlE	Maximum height above the maximal length (PCA)	51.5
BHlE	Height of endobregma above the maximum length	49.5
FalC	Frontal chord (between the base of encephalic rostrum and the intersection between the central sulci and the interhemispheric fissure)	114.5
PalC	Parietal chord (between the intersection between the central sulci and the interhemispheric fissure and the intersection between the perpendicular sulci and the interhemispheric fissure)	63
OalC	Occipital chord (between the intersection between the perpendicular sulci and the interhemispheric fissure and the posterior interhemispheric point)	57
S Fal	Surface of the frontal lobe (values for right and left sides)	73.5/69.8
S PTal	Surface of the parieto-temporal lobes (left side)	94.6
S Oal	Surface of the occipital lobe (left side)	32

lated using the formula $\sum(\sum|Rxi\text{-}Lxi|)/N$, where R is the right side, L the left side, x the value, and i the individual (Palmer 1994). Morphometric data were scaled relative to each individual's endocranial volume; the cube-root of the endocranial volume (EV) for each individual was thus used to scale each linear variable ($(xi/(3\sqrt{EVi})*100)$) or for surface quantification ($(2\sqrt{xi})/(3\sqrt{EVi})*100)$).

GLOBAL SHAPE OF THE SKULL

We carried out an analysis of the exo- and endocranial vault in the mid-sagittal plane using two-dimensional geometric morphometrics. The mid-sagittal plane was defined through a series of 3D cranial landmarks taken on the midline (nasion, glabella, supra-glabellar point, bregma, lambda, and inion) and used to create a cross-section of the skull using Avizo 7. This cross section was then used as a reference to place midline points on the endocast (tip of the encephalic rostrum, intersection of the sagittal and central sulci showing the midsagittal posterior extension of the frontal lobe, intersection of the sagittal and parieto-occipital sulci showing the midsagittal posterior extension of the parietal lobe, and endinion). Projections of the 3D landmarks onto the 2D profile image created with the cross-section tool were then digitized as 2D landmarks. Slidingsemi-landmarks were along the boundary curves of the inner and outer vaults so that each bone and lobe was described through its own set of semi-landmarks. We used Avizo 7 to define the mid-sagittal plane and extract the cross-section, and the TPS suite (Rohlf 2008, 2009) to digitize 2D landmarks and semi-landmarks. All semi-landmarks (exo- and endocranial) were slid simultaneously using the 'bending energy' setting of the gpagen function of the R package geomorph (Adams and Otarola-Castillo 2013). Principal Component Analyses (PCA) of the shape variables computed through our landmark configurations were performed using the R packages Shapes (Dryden 2013) and Morpho (Schlager 2013). Generalized Procrustes Analyses (GPA) were performed before each PCA to superimpose all specimens, removing size,

TABLE 4. CRANIAL VAULT THICKNESS (in mm) OF BH1 AT SOME SPECIFIC POINTS (values are means of several points near the landmark [see text]).*

Landmark	CVT (in mm)	side
Bregma	9.4	
Mid G/B	8.1	
Lambda	11.7	
Pterion	6.2	Left
	6.1	Right
Asterion	12.7	Left
Stephanion	7.8	Left
	7.9	Right
Parietal eminence	11.2	Left
	10	Right
Mid B/L	8.8	

*G: glabella, B: bregma, L: lambda.

location, and orientation effects from the sample. For each individual, the ecto- and endocranial vaults were digitized as a single object on which we performed a PCA.

RESULTS – THE INTERNAL ANATOMY OF BH1

PRESERVATION AND PALEOPATHOLOGY

A small depression is visible exocranially on the left parietal bone at the intersection of its anterior third and at its medial third. It is located along the course of the temporal lines, which are affected by the presence of this depression. It measures 30x15mm, with its long axis parallel to the temporal line, which is also slightly depressed. It seems to impact mostly the external extension of the external table, but not the underlying bone layers. Several lesions also were described on the temporal bone of BH1 (Montgomery et al. 1994). The microCT data helps to visualize the characteristics of all these features in greater detail than before. We agree with previous suggestion that the retromeatal lesion, the mastoid tip lesion, and the petrous lesions are post-mortem defects. However, in contrast to several previous assessments, we consider that the squamous temporal bone lesion also is post-mortem. Indeed, the microCT data clearly reveal that this defect is not associated with any healing or other biological reaction.

VARIATIONS IN CVT AND STRUCTURAL BONE COMPOSITION

Along the mid-sagittal plane (see Figure 2). The maximal thickness at glabella is slightly over 31mm. Bone thickness decreases rapidly posterior to the frontal torus. It then varies on the central third of the frontal bone between 8mm and 9mm. Thickness measured at the center of the glabella-bregma distance (Mid G/B in Table 4) is 8.1mm. Thickness then increases toward bregma, where it reaches a value around 10.5mm anterior to this point. At bregma, the thickness measured directly on the 3D model is 9.4mm. In terms of structural bone composition, the frontal sinuses occupy the anterior third of the frontal bone. Posteriorly, the tables are well differentiated and quantifiable as far as near bregma. In the posterior two thirds of the frontal squama, the proportion of the external table increases antero-posteriorly from around 30% to 45% of total bone thickness, while the proportion of the internal table decreases from 45% to 30%, whereas the diploic layer remains quite stable in terms of relative contribution, with values comprised between 25% and 30%. As a result, the diploic layer is always the least-represented constituent of the posterior part of the frontal squama along the mid-sagittal plane.

Thickness decreases rapidly posteriorly to bregma, reaching 6.6mm at one-third along the parietal bone. It then increases all along the junction of the parietal bones. Thickness is 8.8mm at midway between bregma and lambda (note Mid B/L in Table 4) and 11.7mm at the level of the lambda. Structural bone composition is not quantifiable in the mid-sagittal plane for the parietal bones, as the sagittal suture is patent and therefore the bone tables are not differentiated in this area.

Thickness continues to increase on the occipital bone posteriorly to lambda. It reaches a value of 13mm at the limit of the anterior third of the occipital plane. Thickness then decreases, and increases again when getting closer to the area of the occipital torus. Unfortunately, this last anatomical area is not completely preserved and its thickness cannot be estimated. Finally, the thickness decreases slowly along the nuchal plane. On the occipital plane, the diploic layer is the main component of the total bone thickness, representing around 36–43% of total bone thickness. The external table constitutes around 23–26% and the internal table 33–37%.

For the complete vault (see Figure 3). In the areas where thickness is directly quantifiable between the endo and exocranial surfaces—without going through cranial superstructures and where the surfaces are roughly parallel—the maximum thickness is reached in the glabellar area. The supraorbital torus is particularly well-developed in all directions. It is well isolated antero-posteriorly from the vault, but it also has a continuous and substantial vertical development all along its lateral extension. Another thickened area runs from the mastoid process towards the mastoid crest and the junction with the occipital torus. The thinner areas of the upper vault are located on the most infero-lateral extension of the frontal bone, in the center of the temporal squama and on the nuchal plane.

The frontal bone. The frontal bone is thinner along the antero-posterior course of the first frontal convolution. Areas of minimal thickness, around 5mm to 6mm, closely follow the shape of these endocranial areas. Laterally, thickness is greater as far as the course of the temporal lines. Bone thickness in this area varies between 8mm and 11.5mm, and follows the shape of the underlying second frontal convolutions. Along the lateral walls of the frontal

bone, thickness decreases toward its most infero-posterior corners, where the bone is very thin, around 2mm. This thinner area extends vertically and corresponds exactly to the location of the lateral extension of the third frontal convolution. There is a clear frontal keel on nearly all the frontal squama. It starts in the glabellar area where it is a small relief and enlarges posteriorly in a large bregmatic eminence. The frontal keel is not related unambiguously to variation in overall bone thickness, as it is only slightly elevated above the rest of the external cranial surface, compared to the variations in bone thickness due to larger endocranial traits.

The bregmatic eminence, on the other hand, is an external feature related to a slight increase (~3mm) of the total bone thickness, due to the variation in the endocranial surface associated with the uppermost extension of the first frontal convolution. Thickness is around 10.5mm in the bregmatic area compared to a minimal value of 7.5mm at the lateral border of the eminence on the left side, around 1.5cm from the mid-sagittal area. There is no coronal keel. Bone thickness along the coronal suture is mainly affected by the presence of the suture. Values are therefore lower than anteriorly and posteriorly.

The frontal sinuses play a major role in the internal anatomy of the frontal bone due to their great extension (see below), including invading the anterior half of the frontal squama. In the posterior half, the contribution of the internal table to CVT decreases antero-posteriorly and appears to vary laterally in relation with total bone thickness. The external table is thicker posteriorly and also where bone is thicker. The diploic layer shows more variation, particularly in relation to the pattern of variation of the endocranial topography; whereas the inner and outer bone tables show a general trend of thickness variation of the frontal bone, the diploic layer is the one that varies most in relation to local modifications in bone thickness.

Several foramina are visible on the anterior surface of the frontal torus. They propagate internally and many of them connect with the frontal sinuses. Just posterior to the frontal sinuses and in the medial part of the frontal squama, several foramina on the endocranial surface communicate with the diploic structure of the bone.

Parietal bones. The area of maximal thickness (15mm) is the postero-lateral corner of the bone. This is due to the presence of a marked external ridge, namely the mastoid crest, which continues on the parietal bone and forms an angular torus that connects on the occipital bone with the lateral extension of the occipital torus. The underlying endocranial structure is the lateral sinus and the postero-basal extension of the temporal lobe, which is less projecting than the adjacent middle temporal gyrus or the occipital lobe, contributing to the observed thickening of the bone. The parietal bones are also globally thicker medially, with values comprised between 11mm and 13mm, and thinner at their antero-lateral extension, with a minimal thickness of around 4mm. This pattern of distribution may be explained as follows: the thicker area corresponds to the course of the interparietal sulci and is related posteriorly to the slight development of the parietal lobes (i.e., supramarginal and angular gyri), while the bone is thinner at the lateral border of the parietal bones, where the surface is more vertical. Indeed, the deep imprints of the meningeal system on the endocranial surface in this area imply clear localized thinning of the bone.

At the anterior junction of the parietal bones there is a V-shape area of thinner bone that corresponds to the uppermost extension of the ascending frontal gyri. In addition, Pacchionian impressions accentuate the relief in this area, causing a depression of the endocranial surface and the observed thinning of the bone. This thinning also corresponds to the posterior extension of the bregmatic eminence. There is no exocranial relief at the junction of the two parietal bones, no keel and no parasagittal flattening are observable. On the contrary, the exocranial surface of the bone seems to be flattened all along the extension of the suture. The variation in bone thickness in this area is mainly due to the presence of the sagittal sinus, a depression on the endocranial surface that decreases bone thickness. The slightly thicker area in the posterior half of the junction of the parietal bones is related to the depressions on both sides of this sagittal sinus. The diploic structure of the parietal bone is partly altered in its inferior extension, particularly on the exposed right side and for the inferior half on the left side. There, the diploic bone is highly mineralized, more so than in the inner and outer bone tables, and its internal structure is not perfectly preserved. Above, the structure is visible and some canals for diploic veins are observable.

The relative thickness of the inner and outer tables is consistent along the full extent of the parietal bones. The diploic layer is the component whose contribution to total bone thickness varies the most in relation with total bone thickness. It is the main component where thickness is maximal and it is much thinner when total bone thickness decreases, where it contributes the least to total bone thickness.

Temporal bones. Bone thickness is minimal in the area of most of the lateral course of the middle temporal gyrus (~3–4mm). Maximum values (~12mm) are measured in the anterior corner of the squama, and in and posterior to the mastoid area. The upper part of the squama has a thickness of around 8mm. This area of thicker bone corresponds endocranially to the course of the sylvian valley.

Occipital bone. The course of the internal occipital crest creates a clear thickening of the bone; the maximum value is ~13mm, just posterior to lambda. The thinnest areas of the occipital squama (~4mm) correspond to the endocranial occipital poles. The preserved course of the occipital torus is an area of thickened bone. Due to the incomplete preservation of the central part of the bone, we cannot estimate the thickness at the external occipital protuberance. Thickness reaches a minimal value of 3mm on the cerebellar plane in the preserved areas of the incurvation of the cerebellar fossa. Endinion was certainly below inion.

The distribution of bone thickness is generally symmetrical (with respect to the sagittal plane) all over the vault,

with no large bilateral variations. Some local and restricted variations are visible, however. The clearest asymmetry is observed in the center of the parietal bone, around the area of the parietal eminence. Here, the left side is thicker than the corresponding area on the right. This is due particularly to a slight differential development of the underlying endocranial structures.

Additional metrics for CVT. The thickness of the frontal bone on a circular area of 1.2cm in the center of the frontal bone has a mean value of 7.7mm there. In this area, the mean thickness of the external table is 2.3mm, the mean value for the diploic layer is 2.5mm, and the mean value for the internal table is 2.9mm. On the left parietal bone, a circular area of 2.5cm in the center of the bone has a thickness with a mean value of 10.9mm. In this area, the mean thickness of the external table is 2.7mm, the mean value for the diploic layer is 6.1mm, and the mean value for the internal table is 1.8mm. Additional values were quantified for standard anatomical landmarks (see Table 4).

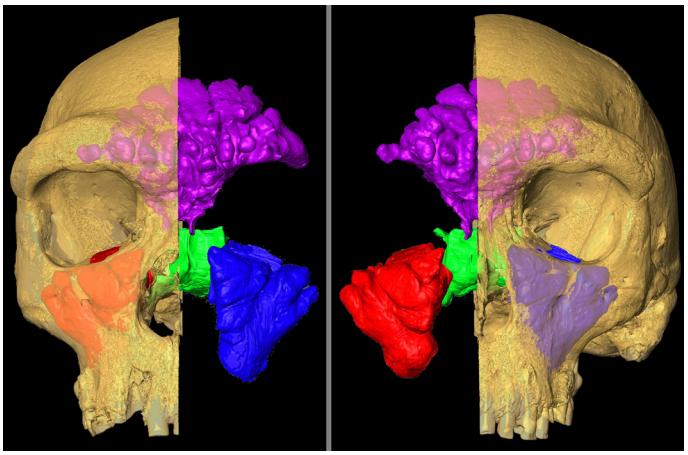

Figure 6. Virtual reconstruction of BH1 cut away to display sinuses sectioned out and shown as colored volumes (colors as in Figure 5). Not to scale.

TOOTH ROOTS

Anterior tooth roots. The metric data are shown in Table 1. The roots of the upper central incisors show an approximately circular section at the cervical line (R ratio (LL) / R (R): 0.9 – 1.0 for the right central incisor and 1.1 for the left) and retain this form throughout their length. No mesial or distal groove is seen. Because of the partial obstruction of the pulp cavity of the right central incisor by a secondary deposit (calcite or secondary dentine), the RPV (root pulp volume) is clearly different between the two central incisors (CV: between 0.3mm³ and 8.2mm³ for the right incisor and between 11.5mm³ and 21.3mm³ for the left incisor). Due to the same kind of deposit located at the extremities of the tooth, the pulp cavity volume of the left central incisor is also underestimated. In the side view, the labial and lingual surfaces are approximately straight from the apex to the cervical line.

The root of the upper left lateral incisor has a more oval cross section (ratio R(LL) / R(MD): 1.3) at the cervical marginal line than the central incisors, and retains this form throughout its length. This root is characterized by the presence of a mesial and distal shallow groove, which takes shape only on the middle third of the root. The pulp cavity is visible over the entire length of the root, with the exception of the apical extremity and the RPV is 13.8mm³. In side view, the labial surface of the root is convex from the apical extremity to the cervical marginal line, while the labial surface is approximately straight.

The upper canines present a more oval cross-section than the incisors (ratio R(LL) / R(MD): 1.4 for the left canine) at the cervical marginal line, and retain this shape throughout their length. The right canine has a fracture of the root under the cervical marginal cervical line, which greatly limits the available metrical data for this tooth. In the side view, the labial surface of the root of the canines shows a concavity on the lower one-third and a convexity on the upper two thirds, while the labial surface is relatively straight. In vestibular view, both canines have an apex that is oriented distally compared to the main axis of the root. The RPV of the right canine (31.2mm³) is underestimated due to the obstruction of the apical pulp by a secondary deposit.

Postcanine tooth roots. The premolars of the BH1 specimen have only one root. However, the third premolars differ from fourth premolars by the presence of a deep and extensive mesial groove, which is more pronounced on the right. The pulp cavity of the right third premolar has two canals throughout the length of the root, while the root pulp of the left third premolar is bifurcated only in the central third of the root. The roots of both fourth premolars are devoid of mesial or distal grooves and have only one pulp canal.

The molars have three roots, with the exception of the right third molar which possesses only two. However, the vestibular root is marked by a strong groove and the vestibular canal pulp is bifurcated. Thus, all of the upper molars of BH1 have three pulp canals. The pulp chambers of the second molars are the best preserved of all and have a total volume of 27.29mm³ for the right tooth and 34.83mm³ for the left. One part of the crown and the root of the left second molar is absent at the mesial side due to a carious lesion. The coronary pulps have a sub-triangular shape in occlusal view and have two cusps marking the location of the paracone and protocone.

PNEUMATIZATION

Paranasal pneumatization. The frontal, maxillary and sphenoidal sinuses of BH1 are shown *in situ* (Figures 6 and 7); their sizes, measured by volume and surface area, are shown in Table 5 and their extents are given in Table 6. The relative extents of sinuses measured from virtual reconstructions (as here) is difficult to compare between specimens, due to the difficulty of standarizing orientation between virtual specimens. Thus, the data presented here are intended only to enable visualization of the size of the sinuses within the cranium (a relationship that is difficult to

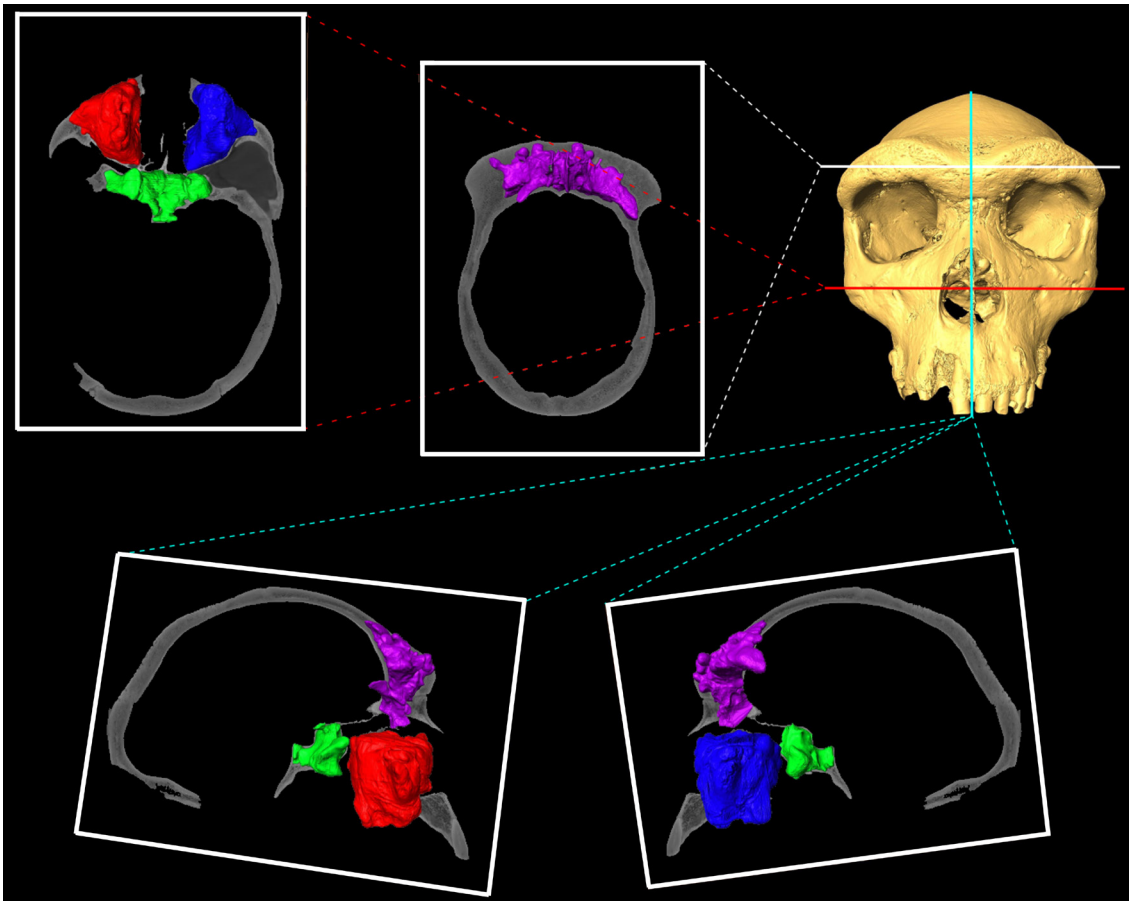

Figure 7. MicroCT slices through BH1 exposing sectioned out sinuses, which are shown as solid, colored volumes. Top right: virtual reconstruction from CT data with colored lines showing slice locations. White: transverse slice showing frontal sinus; red: transverse slice showing maxillary and sphenoidal sinuses; blue: sagittal slice showing frontal, maxillary, and sphenoidal sinuses from right (left hand slice) and left (right hand slice) slides. Not to scale.

infer from volume and surface area measurements alone); these measurements are not compared to those from other fossils. Only left maxillary sinus extent is reported, as there is little bilateral asymetry in maxillary sinus size (Buck 2014).

A single, undifferentiated frontal sinus fills the antero-posterior length of the very large supraorbital torus and extends laterally to beyond the mid-point of each orbit; the sinus also extends posteriorly far into the sloping frontal squama towards bregma and inferiorly extends past nasion. The overall shape of the frontal sinus is fan-like, but is made up of many small globular, coral-like extensions filling the entire depth of the bone thickness. This complex shape is visible in its full detail for the first time via high-resolution microCT data. Although this specimen shows a single, continuous frontal sinus, pneumatization extends further laterally on the left side than the right. The maxillary and sphenoidal sinuses are far less complex in shape than the frontal sinus, largely conforming to, and filling, the respective bones they pneumatize. The maxillary sinuses are roughly inverted pyramidoidal in shape, with shallow division into several lobes laterally and anteriorly. The sphenoidal sinus fills the body of the sphenoid and spreads into the greater sphenoidal wings, extending further on the right side than the left.

TABLE 5. SINUS METRICS FOR BH1.*

Sinus	Frontal			L. maxillary			R. maxillary			Sphenoidal		
Measurement	**Vol**	**SA**	**S/V**	**Vol**	**SA**	**S/V**	**Vol**	**SA**	**S/V**	**Vol**	**SA**	**S/V**
	38478.6	14604.1	0.4	38050.7	8142.3	0.2	39978	9079.2	0.2	16466	6847.7	0.4

*Vol: volume (mm^3), SA: surface area (mm^2), S/V: surface area to volume ratio

TABLE 6. MEASUREMENTS OF SINUS EXTENTS FOR BH1 (mm) (see Figure 5).

Measurement	Sinus		
	Frontal	Left Maxillary	Sphenoidal
Glabella towards bregma	50.1		
Glabella towards left frontomalare temporale	51.5		
Glabella towards right frontomalare temporale	42.9		
Glabella towards nasion	29.0		
Left alare towards nasion		28.2	
Left alare towards C/P3		28.1	
Left alare towards left zygomaxillare		47.3	
Left alare towards left molars posterior		52.7	
Hormion towards left foramen ovale			30.8
Hormion towards right foramen ovale			39.3
Hormion towards basion			19.2
Hormion towards prosthion			19.9

Temporal bone pneumatization (Figure 8). The temporal pneumatization is well preserved inside the left temporal bone, except where a hole (see above) penetrates the antero-superior portion of the mastoid process. Air cells are exposed at the bottom of this cavity, but also at the lowermost extension of the mastoid process and at the postero-medial extension of the superior surface of the petrous bone. The volume of the preserved pneumatization is 5.4cm^3. Based on the size of the hole (0.6cm^3), the estimated original volume of the temporal pneumatization probably did not exceed 6cm^3.

The antrum is large and the corresponding air cells extend from this cavity, particularly in planar view. Pneumatization is well developed in the petro-mastoid area. Anteriorly, cells are present as far as above the external auditory meatus. Superiorly, the pneumatization is limited to the uppermost extension of the petrosal; cells do not invade the squamous temporal. Inferiorly, cells are present in the anterior part of the mastoid process, reaching the most inferior extension of this process, but are only present in the more anterior and uppermost extension of the juxtamastoid eminence. Medially, some air cells reach the apex of the petrosal; they are also the most anterior and superior portions of the temporal bone. Posteriorly, some pneumatic cells, located in the summit of the mastoid, reach the level of the parietal notch. The cells are globally larger inferiorly than superiorly; this is particularly true for the mastoid area and the basal part of the petrous bone, where cells are larger than those observed above the level of the external auditory meatus and when closer to the petrosal apex.

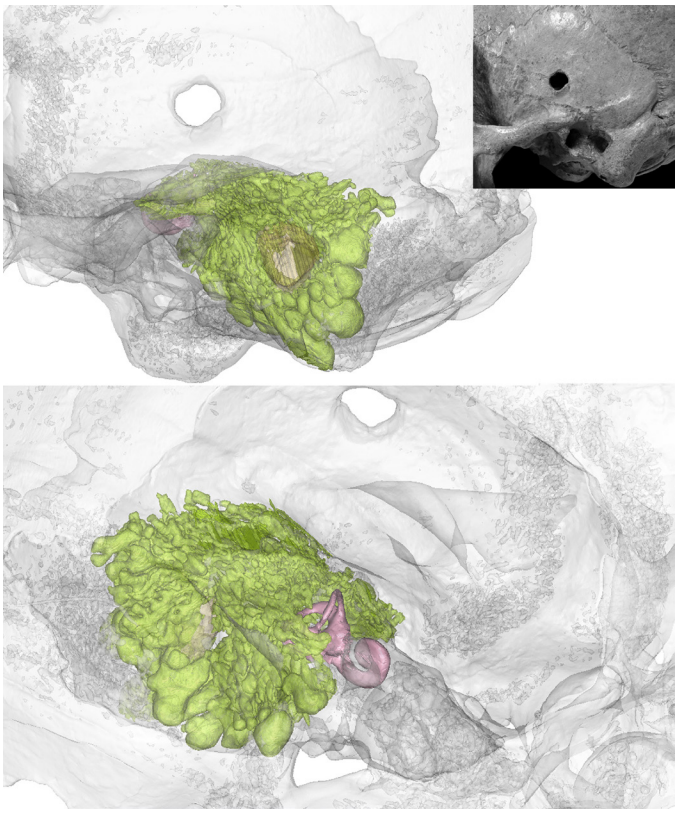

Figure 8. The left temporal bone of BH1 and 3D reconstructions in left lateral and endocranial views where the bones are shown in grey; pneumatization is visible by transparency and is shown in darker color as well as the cochlea and semi-circular canals.

ENDOCAST AND BRAIN ANATOMY (FIGURE 9)

Endocranial volume for BH1 has been estimated previously between 1259cm^3 and 1325cm^3 (Elliot Smith 1928; Holloway et al. 2004; Seidler et al. 1997). Here, the virtual reconstruction of the BH1 endocast produced via mirror imaging of the missing parts from the existing areas on the contralateral side has a volume of 1280cm^3, remarkably similar to the first estimation published (Elliot Smith 1928). The extreme values previously published for this individual show a variation of less than ±3%. This value of 1280cm^3 for the endocranial volume of BH1 is used in the rest of this article and can be considered as a reliable estimation for this specimen in future works.

Overall morphology. The endocast is elongated, wide and low. The maximum width is in a low position at the level of the temporal lobes, but with a relatively anterior position in the median portion of the temporal lobes; as a result, the endocast is ovoid in shape in superior view. The supramarginal gyri constitute a clear relief, meaning that the endocast seen in posterior view has lateral walls that are weakly convergent towards the top. In lateral view, the sagittal curvature is convex as far as the middle part of the parietal lobes; there it forms a depression that continues towards the perpendicular sulci in front of the occipital lobes. Standard measurements for this endocast are given in Table 3.

Vascular impressions. The superior sagittal sinus is visible between the frontal lobes in an attenuated form. Its diameter increases from the area of the central sulci towards the occipital lobes; it continues there in the right lateral sinus, which is only partly preserved. The left lateral sinus is visible in the area of the confluence of the sinuses, where it has a smaller diameter compared to the right sinus. Its diameter increases regularly all along its course toward the sigmoid sinus. This last sinus is preserved throughout its length as far as the anterior part of the left cerebellar lobe. Three granular foveolae are located in the anterior part of the frontal lobes, one on the right side of the superior sagittal sinus and two on the left; all are located at the level of the anterior rami of the middle meningeal system. There is no evidence of the sphenoparietal sinuses. The left superior petrosal sinus forms a shallow depression. The structure that borders the foramen magnum may correspond to the left marginal sinus.

The general pattern of the meningeal vessels is similar on both hemispheres. The anterior ramus is the more developed, covering the posterior part of the frontal lobes and the complete parietal lobes. On the left hemisphere, the common tract is visible from the base of the temporal lobes. At the lateral extent of the junction of the middle and anterior fossae, which also corresponds to the junction of the frontal and sphenoid bones, the vessel penetrates the bone to a small extent (~5mm). This explains why this vessel is not visible on the endocast just above the sylvian valley. This feature implies a strong integration during growth and development of the brain, the meningeal system and the skull.

The common tract of the meningeal vessels splits into three unequal branches along its course. The anterior (or bregmatic) branch is the most prominent and has the widest diameter. At first, this branch follows the course of the lateral sulcus; it then has a more vertical orientation and splits in several branches that also show several rami. The anterior ramus is well developed with long imprints that make some anastomoses together; these are less numerous on the left side. The obelic branch has a reduced diameter in its anterior extension. It is parallel to the posterior branch as far as the posterior part of the supramarginal gyrus, where it splits into two rami. The posterior (or lambdatic) branch is also reduced, but is the first to separate from the common tract along the temporo-cerebellar excavation. It shows some rami at the level of the superior part of the third temporal convolution.

The general orientation of the middle meningeal system is oblique. On the right hemisphere, the surface corresponding to the anterior branch is preserved and a similar pattern to that on the left is observed; it also penetrates the bone for a few millimetres. This branch, however, also is divided into an anterior section that is present for 1.5cm anteriorly. It leaves the bone in the center of the sylvian valley, just behind the third frontal convolution.

In addition, some imprints of the anterior meningeal system are visible in the anterior part of both hemispheres. They are numerous and very thin. They cover the lateral extension of the third frontal convolution in the direction of the head of this convolution, reaching the middle part of the second frontal convolution with a tree-like structure. Finally, thin imprints are also visible on the encephalic rostrum.

Sulcal and gyral imprints. On the frontal lobes, the transverse curvature is regularly convex. The interhemispheric sulcus is narrow. The encephalic rostrum is short and large. The anterior parts of the first frontal convolution that constitutes this rostrum are larger on the right side. The orbital part is exceptionally well preserved and concave on both sides. In anterior view, the orientation of the orbital part is horizontal, joining laterally the basal part of the third frontal convolution on both sides. This morphology is similar to that observed in *H. sapiens*.

On the inferior surface of the frontal lobes, only those imprints corresponding to the right orbitofrontal sulci are visible. On the left side, the corresponding sulci have a disorganized distribution and the external and internal orbital sulci cannot be discerned unambiguously. The optic chiasm and the adjacent areas of the optic tracts are well preserved. A circular protuberance in the center of the chiasm could correspond to the imprint of the hypophysis.

The superior surface of the frontal lobe displays numerous depressions corresponding to the frontal sulci that delimitate the three frontal gyri. The width of the first frontal convolution increases from the frontal pole to the ascending frontal gyrus. The anterior limit of the ascending frontal gyrus is not clear and is probably located in the area of the first frontal convolution at the level of the imprint of the coronal suture. The imprints that delimit the third fron-

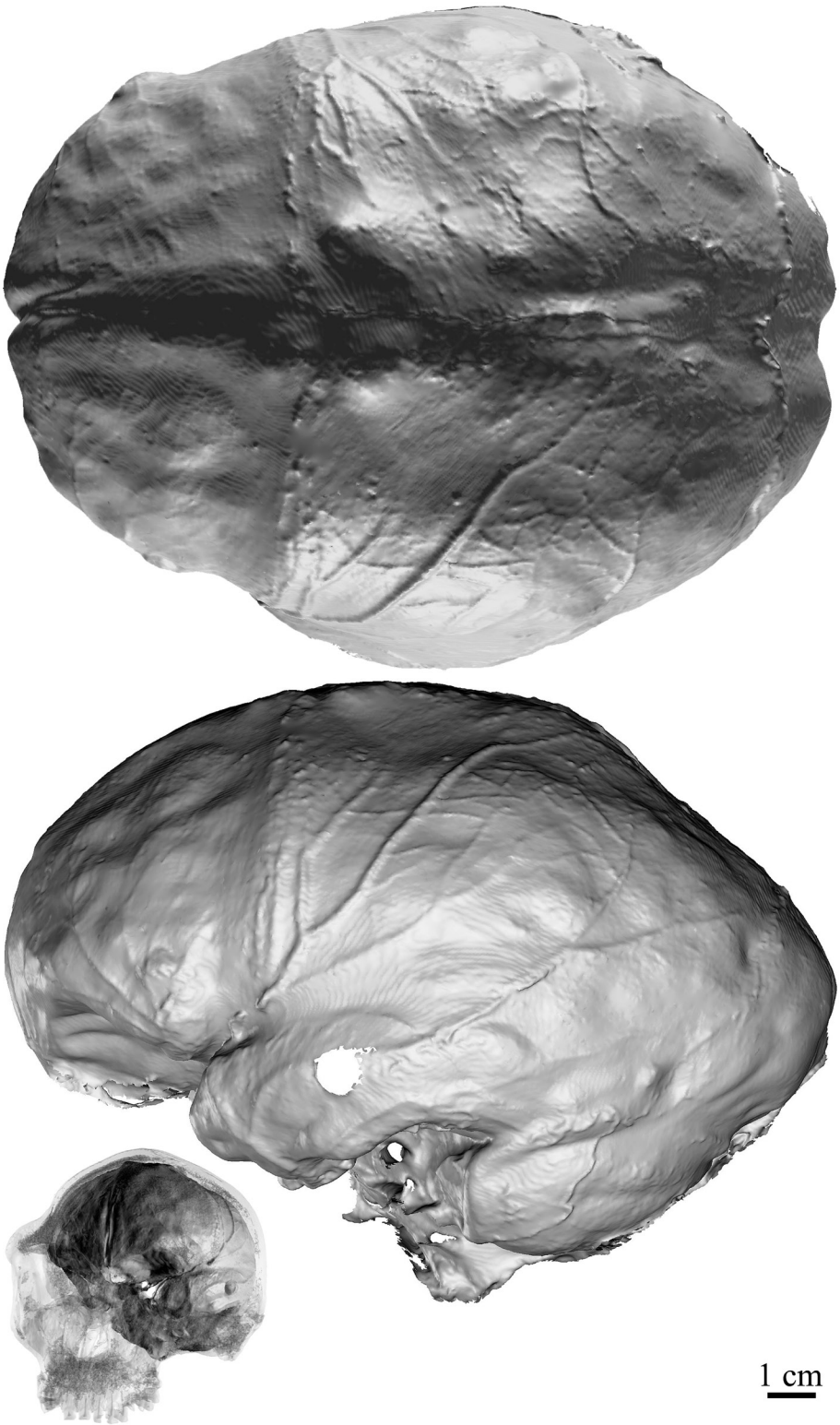

Figure 9. 3D models of the endocast of BH1 in superior and left lateral views. Representation in antero-lateral views of the 3D reconstructions of the skull shown by transparency and of the endocast.

tal convolution are well marked. The cap incisure depresses the center of this convolution on both hemispheres. The third frontal convolution is more pronounced and projects more laterally on the right side, which is possibly related to a lesser connection with the temporal pole; as a result, the width between the frontal and the temporal lobes is wider on the right hemisphere.

The sylvian valley between the frontal and the temporal lobes continues into the lateral sulci, whose orientation is horizontal. On the right side, the lateral sulcus corresponds to the inferior limit of the preserved part of the endocast. The height of the left temporal lobe is identical from the pole to the parietooccipital sulcus. The imprint of the superior temporal sulcus is barely perceptible and the one for the inferior temporal sulcus follows the inferior border of the lobe. The temporal gyri are therefore not perfectly individualized all along their extension.

In the parietal lobes, the transversal curvature is maximal at the supramarginal gyri, depressed at the level of the interparietal sulcus and strongly convex in the area of the first parietal convolutions. These last are separated from each other by the width of the superior sagittal sinus. On both sides, the central sulcus is difficult to identify. Conversely, the post-central sulci are easy to locate thanks to the clear anterior limit of the supramarginal gyri on both sides. The reliefs of the angular gyri are difficult to delimitate from those of the supramarginal gyri because the intermedius primus (Jensen) sulcus is not visible. The foot of the second parietal convolution is circular in shape and well separated on the left side, but not preserved on the right hemisphere. The second parietal convolutions, where they are bilaterally preserved, have a similar pattern.

The occipital and cerebellar lobes are preserved on the left hemisphere. The occipital lobe is prominent, accentuated by the depression in the posterior part of the parietal lobes. The inferior parts of the occipital sulci are clearly visible and separate the three occipital convolutions. These convolutions are not discernible in the upper part of the occipital lobe. The preoccipital incisura is covered by the transverse sinus. The parieto-occipital sulcus is apparent from the pre-occipital notch on both sides, anterior to the lambdoid suture. The cerebellar lobe has an anterior position, being equally located below the temporal and occipital lobes. The horizontal fissure is the only imprint visible on the cerebellar surface.

Asymmetry. Concerning the pattern of fronto-occipital petalia, the BH1 endocast has a right frontal lobe that is more anteriorly projecting, is below, and has a more lateral position relative to the mid-sagittal plane of the skull compared to the left pole. The left occipital pole has a more posterior projection, is above, and has a more medial position relative to the mid-sagittal plane compared to the right pole. These bilateral variations, however, are very small; less than 1mm for the antero-posterior variations and below 4.5mm for the other components of the petalia. Total asymmetry (FA11) for the petalia of BH1 is 8.9mm, compared to a mean of 19.2mm for *H. sapiens*, 15mm for fossil hominins (including several taxa) and 9mm for extant non-human African great apes (Balzeau and Gilissen 2010; Balzeau et al. 2012). This pattern is known to be most common in right-handed humans (e.g., Galaburda et al. 1978; Kertesz et al. 1990; LeMay 1977). The third frontal convolution is located more posteriorly, inferiorly, and laterally on the left hemisphere compared to the right side. The whole area has a more compact shape on the left side. Its size is in the upper part of the range of variation observed for fossil hominins (Balzeau et al. 2014).

RESULTS – COMPARATIVE MORPHOLOGY

COMPARISONS OF BH1 CVT AND STRUCTURAL BONE COMPOSITION

To put the CVT of BH1 into context, a sample of 570 adult recent *H. sapiens* has a mean thickness value of 5.8mm (SD=1.363mm) in the center of the frontal bone and of 5.8mm (SD=1.260mm) in the center of the parietal bone (Copes 2012). These results correspond closely to the mean values obtained by Marsh (2013) on a similar sample (n=138). BH1 (see Table 4) has a significantly thicker frontal bone than the *H. sapiens* sample of Copes (2012) ($p<0.05$); 94.2% of the comparative sample have thinner bone in this area. The same holds for the parietal ($p<0.01$, thicker than 99.1% of the human sample).

Moreover, the *H. sapiens* sample (Copes 2012) has a ratio of diploë/total thickness of 0.429 (SD=0.126) and 0.491 (SD=0.098) for the frontal and parietal, respectively. The values calculated on BH1 are 0.32 and 0.56 for the same bones; these are within the range of variation of parietal composition and total thickness for human frontal and parietal bones (Copes 2012: 113) but at the limits of high thickness values and relatively low diploic ratios. As observed along the mid-sagittal plane (see Figure 2), the diploic layer is relatively thin in the upper part of the frontal squama. It is relatively thicker along the occipital squama, but still represents less than 50% of total bone thickness in this area. This pattern is not different from the variation previously described for *H. erectus* or *H. sapiens*. Only few comparative data, however, are available for fossil hominins (Balzeau 2005, 2006) and this topic will require further investigation to identify possible features of taxonomic relevance.

Our recent comparative analyses of CVT (Balzeau 2013) have shown that BH1, together with Petralona, had the thickest vault observed in our fossil hominin samples. This was observed both for absolute and relative values. Along the mid-sagittal plane, the bone is very thick at the supraorbital torus and then decreases rapidly. An increase in bone thickness along the junction of the parietal bone is also noticeable. The ectocranial relief visible on BH1 is not related to variations in bone thickness; the same pattern has been observed for the frontal keel in several Neandertal specimens and in Petralona (Balzeau 2013). A clear increase in bone thickness was observable only in some *H. erectus* fossils, particularly the most robust ones with more marked external relief. Unfortunately, good data are not available for some of the biggest Indonesian *H. erectus*, nor Lantian or Yunxian, among others.

More generally, the pattern of CVT distribution in BH1, as shown in Figures 3 and 10 is characterized by relatively thicker parietal bones, particularly in the postero-medial area. This feature resembles the morphology observed in *H. erectus sensus lato*. It corresponds to a plesiomorphic expression, whereas the morphology observed in Neandertals and *H. sapiens* correspond to two derived conditions (Balzeau et al. 2013). BH1 and Petralona display the darker range of color in the 3D topographic map (see Figure 10), reflecting the very thick cranial bone in these specimens (Balzeau 2013). They share with *H. erectus* a thick frontal torus or a thickened postero-lateral parietal bone (see Figure 10). Unfortunately, comparative data for early European hominins such as the skulls from La Sima de los Huesos are currently unavailable. The scan set for Petralona is of relatively low resolution, but this specimen also shows high absolute values for CVT and seems to show a pattern of distribution that resembles the plesiomorphic condition observed for BH1. The main peculiarity of BH1 is related to its large, thick frontal torus and to high thickness values for the vault.

TOOTH ROOTS

The length, surface area, and volume of the roots of the anterior teeth of BH1, as well as the cervical diameters and surfaces, correspond to the highest values of the Neandertal sample and are well outside the range of variation of the modern human samples. This observation is true for the various virtual cutting planes used in this study. The length and volume of the incisor roots observed on BH1 also are close to the values recorded for the KNM-WT 15000 specimen, specifically for the lateral incisor (Table 7). However, the pathological state of the teeth of BH1 may have caused hypercementosis, which increases the size of the roots, mainly on the radicular apex. This secondary deposit has not been recognized on the microCT slices of BH1. In general, this deposit seems not exceed a few millimeters of thickness on the apex, particularly for the anterior teeth of Neandertals (Le Cabec et al. 2013), which were subject to high occlusal loads, according to some authors (Brace 1962, 1975; Le Cabec et al. 2013; Smith 1976; Smith et Paquette 1989). Thus, the overestimation of dimensions of the roots caused by hypercementosis can be considered negligible, especially for the linear and surface area parameters.

PNEUMATIZATION

Paranasal pneumatisation. We compared the pneumatization of BH1 to two other important mid-Pleistocene hominin fossils—Bodo and Petralona (Figure 11). Neither Bodo nor Petralona preserves a full complement of the three types of paranasal sinus addressed here; however, both the frontal sinus and one maxillary sinus are measurable in all three specimens. There is a considerable level of variation in sinus volume between these three individuals—Petralona has far larger paranasal sinus volumes than Bodo, which in turn has far larger volumes than BH1, particularly for the frontal sinuses (Table 8, see Figure 11). The differences between specimens also varies with paranasal sinus type; the frontal and maxillary sinus volumes are very similar in BH1 (practically indistinguishable in the case of the frontal and left maxillary), whilst there is a noticeable difference between the frontal and right maxillary sinus volumes in Bodo and a large difference between the frontal and left maxillary sinus in Petralona. These relationships hold broadly for surface area, as well (see Table 8, see Figure 11).

Bodo has a smaller frontal sinus surface area than might be expected from the other two fossils, but this may be due to poor CT scan resolution (clinical rather than microCT). The results presented in Table 9 and Figure 5 also give the impression that the sinuses of BH1 are more complex in shape than its conspecifics, having greater surface area to volume (S/V) ratios, but this may well be due to the greater resolution of the BH1 scan, which enables more accurate segmentation of the sinus for this specimen. It is probably not appropriate to compare S/V ratios between paranasal sinus types (rather than between specimens); if, as seems probable, the sinuses opportunistically expand to fill their respective bones (e.g., Blaney 1990; Buck 2014; Moss and Young 1960; Shea 1977; Vinyard and Smith 1997; Zollikofer et al. 2008), then the more complex shape of the sphenoid bone would be expected to lead to a more complex sinus than that of the frontal.

Temporal pneumatization. Knowledge about the variation of temporal bone pneumatization in hominins is limited, due to the lack of descriptive data available, but a distinctive pattern has been described for Neandertals (Balzeau and Radovčić 2008), whereas more variation has been reported for *H. sapiens* and between different geographic and chronological samples of *H. erectus* (Balzeau and Grimaud-Hervé 2006). The temporal pneumatization in Petralona is more extensive than in BH1, with large cells reaching the central part of the squamous temporal. The pneumatization in BH1 is more developed than in Neandertals, resembling *Homo erectus* in this feature.

ENDOCAST AND BRAIN ANATOMY

Six standard endocranial measurements of the endocast of BH1 (see Table 3) and a large sample of fossil hominins (Balzeau et al. 2013; Grimaud-Hervé 1997; Grimaud-Hervé and Lordkipanidze 2010) were subjected to PCA (Figure 12). These measurements describe the overall shape of the endocast in all directions and have been selected for their utility in discriminating between hominin species. The analysis includes the maximum length, width, and height, as well as the frontal chord, the parietal chord, and the occipital chord. All variables were scaled relative to endocranial volume. The loadings of these variables are illustrated in Figure 12. BH1 (the square in the center of the figure) plots at the limit of the distribution of the *H. sapiens* sample that is located on the bottom left of the chart, and of the other fossil hominins that are on the right. Compared to the mean for *H. sapiens*, the endocast of BH1 is relatively longer, wider, and shorter. It shares this relatively extended length with the other fossil hominins, but it is relatively wider and lower than the rest of the sample. The main difference between BH1 and *H. sapiens* is that the former has a relatively

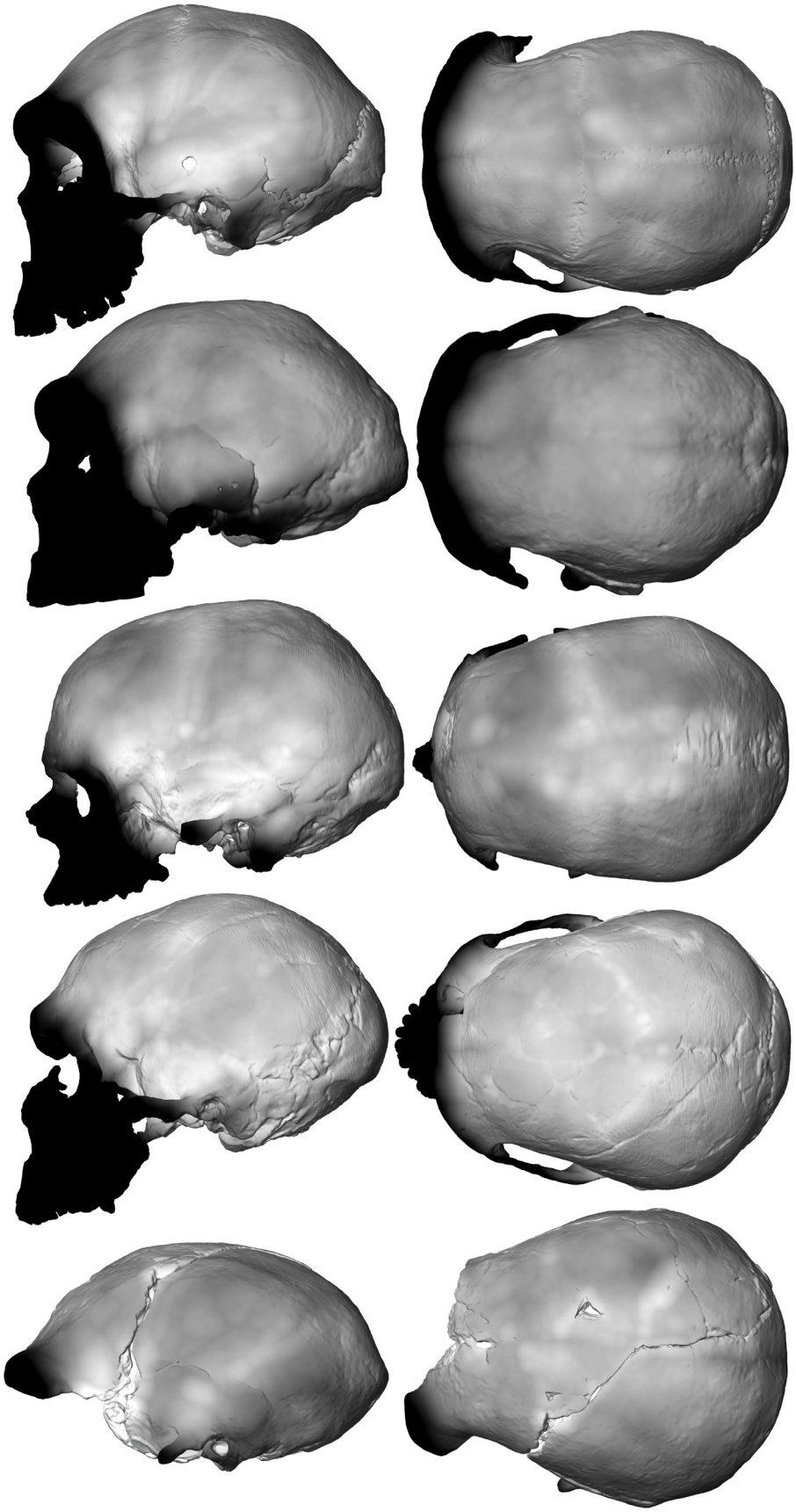

Figure 10. 3D topographic mapping of the variation of total bone thickness rendered using a chromatic scale (thickness increasing from white to black, corresponding to a variation between 2mm and 22mm) in left and superior views in BH1, Petralona, Cro-Magnon 1, La Ferrassie 1, and Sangiran 2.

TABLE 7. LINEAR, SURFACE AREA AND VOLUMETRIC PARAMETERS OF THE COMPARATIVE SAMPLE (from Le Cabec et al. 2013).

Tooth	Taxa	n	RL* (mm)	R(MD)* (mm)	R(LL)* (mm)	RSA* (mm²)	CA* (mm²)	RV* (mm³)	RPV* (mm³)	R(MD)/R(LL) -
UI1	African *H. erectus*	1	20.35	8.53	8.56	407.49	59.86	664.10	49.62	1.0
	Asian *H. erectus*	1	15.40	7.23	6.62	269.06	36.37	364.75	18.70	0.92
	EMH	3	16.61	7.03	7.14	265.76	36.75	346.74	18.21	1.03
	NEA	17	17.23	7.04	7.58	315.31	41.88	452.00	37.25	1.09
	UPEPIH	6	13.50	6.81	6.86	220.25	36.04	274.95	10.87	1.01
	RMH	24	12.94	5.88	6.33	192.33	29.93	225.60	8.74	1.08
UI2	African *H. erectus*	1	18.84	5.01	8.33	425.32	36.61	464.92	27.32	1.66
	EMH	3	15.08	7.03	7.14	230.04	36.75	266.53	21.66	1.38
	NEA	18	17.62	6.11	7.96	343.08	39.59	487.24	31.36	1.31
	UPEPIH	6	13.70	4.78	6.20	188.35	22.90	193.01	7.74	1.3
	RMH	22	12.98	4.60	5.87	172.11	22.01	172.22	6.90	1.28
UC	Asian *H. erectus*	2	21.60	7.20	11.09	501.16	63.55	811.87	67.02	1.54
	EMH	3	18.19	6.26	8.74	315.30	42.53	426.43	28.79	1.39
	NEA	12	22.51	6.18	9.35	454.30	46.18	650.57	36.65	1.51
	UPEPIH	8	16.90	5.71	8.68	278.24	27.11	343.56	16.36	1.52
	RMH	12	16.07	5.31	7.63	254.20	21.97	308.10	9.54	1.44

* RL: root length; R(MD): mesio-distal root diameter; R(LL): labio-lingual root diameter; RSA: root surface area; CA: cervical area; RV: root volume; RPV: root pulp volume; UI: upper incisor; UC: upper canine; BH: Broken Hill; EMH: early modern humans; NEA: Neandertals; UPEPIH: Upper Palaeolithic and Epipaleolithic/Mesolithic humans; RMH: recent modern humans.

low value for the parietal chord; a long parietal chord is characteristic of *H. sapiens*. There is no clear separation between fossil hominin species in this analysis of general dimensions of the endocast. As a group, Asian *H. erectus* specimens fall on the right side of the distribution of fossil hominins, while African specimens, including early *Homo*, are closer to BH1. Neandertals are scattered throughout the fossil hominin distribution.

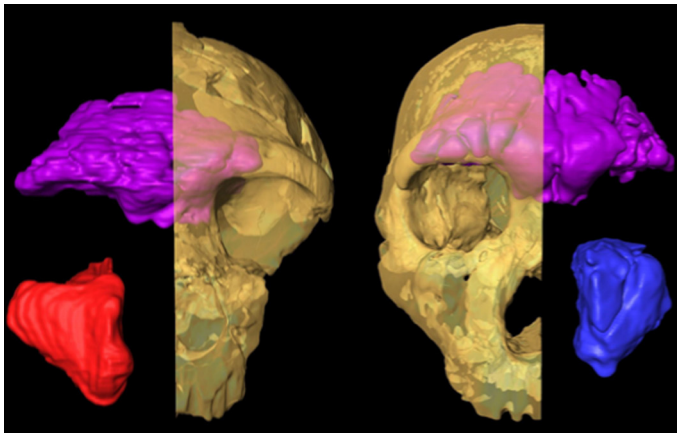

Figure 11. All preserved sinuses in (left to right) Bodo and Petralona. Frontal: magenta; right maxillary: red; left maxillary: blue. Not to scale.

The relative values for the surface area of the different lobes in BH1 are 110.2 for the frontal lobes (based on the values for both hemispheres), 126.7 for the parieto-temporal lobes (from the value obtained on the left side), and 73.7 for the occipital lobes (also derived from the valued measured on the left hemisphere). Comparative data for several fossil hominin species have already been published for this feature (Balzeau et al. 2012; Grimaud-Hervé 1997), and BH1 falls within the range of variation of the *H. erectus* samples for the relative surface of the frontal lobes, of Asian *H. erectus* for the parieto-temporal lobes, and of all the fossil samples for the occipital lobes. BH1 has a relative value for the parieto-temporal lobes that is significantly smaller ($t=-3.302$, $p<0.001$) than the mean for *H. sapiens* (mean=141mm, n=106).

GLOBAL SHAPE OF THE SKULL

This morphometric analysis provides additional data about some cranial features and their related internal variations, both of which have been suggested to be diagnostic of the "mid-Pleistocene assemblage" (Rightmire 2001, 2004, 2013).

We performed a first analysis on the whole sample (fos-

TABLE 8. SIZE-CORRECTED SINUS MEASUREMENTS USING G-FMT (glabella to frontomalare temporale).*

	Frontal		L. maxillary		R. maxillary		Sphenoidal	
Specimen	**Vol**	**SA**	**Vol**	**SA**	**Vol**	**SA**	**Vol**	**SA**
BH1	84.0	245.7	83.0	137.0	87.2	152.7	35.9	115.2
Bodo	145.1	243.3			123.8	159.5		
Petralona	208.73	378.94	141.23	177.36				

*Measurements in mm^3 for volumes and mm^2 for areas. Broken Hill 1 measurements taken from microCT data as above, Bodo and Petralona measured on medical CT scans with resolutions of 0.5mm x 0.5mm x 1mm, and 1mm x 1mm x 1mm, respectively, data from institutions in the acknowledgements.

TABLE 9. SIZE-CORRECTED SURFACE AREA TO VOLUME RATIO FOR EACH PRESERVED SINUS FOR BROKEN HILL 1, BODO, AND PETRALONA.

Specimen	Frontal	L. maxillary	R. maxillary	Sphenoidal
	S/V	**S/V**	**S/V**	**S/V**
BH1	2.93	1.65	1.75	3.21
Bodo	1.68		1.29	
Petralona	1.82	1.26		

sil species and *Homo sapiens*), and a second analysis on the fossil taxa only (n=17), in order to gain a better understanding of profile variations within the genus *Homo* when removing the globularization phenomenon seen in *H. sapiens* from the analysis.

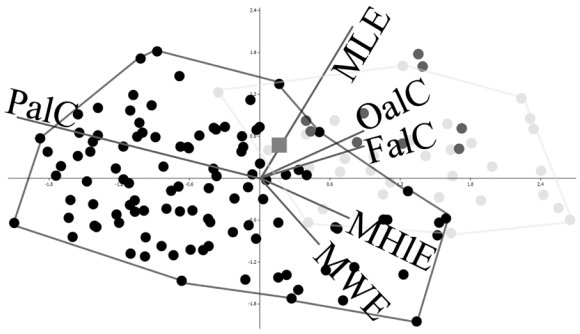

Figure 12. First and second principal components (representing respectively 47% and 22.8% of the total variance) computed on the size-corrected variables maximum length of the endocast (MLE), maximum width (MWE), maximum height above the maximal length (MHlE), frontal chord (FalC), parietal chord (PalC), and occipital chord (OalC). The black circles correspond to the recent modern humans, the dark grey circles to the fossil Homo sapiens and the light grey circles to the fossil hominins. BH1 corresponds to the large grey square.

The PCA of the data for the whole sample (Figure 13) shows a clear separation between *H. sapiens* and other species of *Homo* along PC1, which accounts for 41.2% of the total sample variation. Fossil specimens also show some separation along PC2 (32.2% of total sample variation), with the Chinese and more recent Indonesian *H. erectus* clustering respectively at the positive and the negative end of the axis. Neandertals, the older Sangiran 2 fossil, the two African *H. erectus* fossils, Petralona and Broken Hill 1 are intermediate, with Neandertals nevertheless grouping together within this cluster. The greatest part of the variation in this sample according to this PCA is accounted for by the differences between *H. sapiens* and other species of *Homo*. Changes in the shape space include a drastic reduction in the frontal and occipital superstructures, a globularization of both the skull and endocranium with a vertical development of the parietal lobes and bones, and a more retreating position of the tip of the encephalic rostrum. Another important portion of the variation in this sample is accounted for by the variables of PC2, which separates the three main clusters of fossil specimens (Chinese and Indonesian *H. erectus* at the two extremes of the axis, and the other fossils clustering together in an intermediate position). This shows (from negative to positive values) a further reduction in frontal and occipital superstructures caused by a more projecting occipital lobe, relatively shorter frontal bone and lobes, and relatively longer parietal bones and lobes.

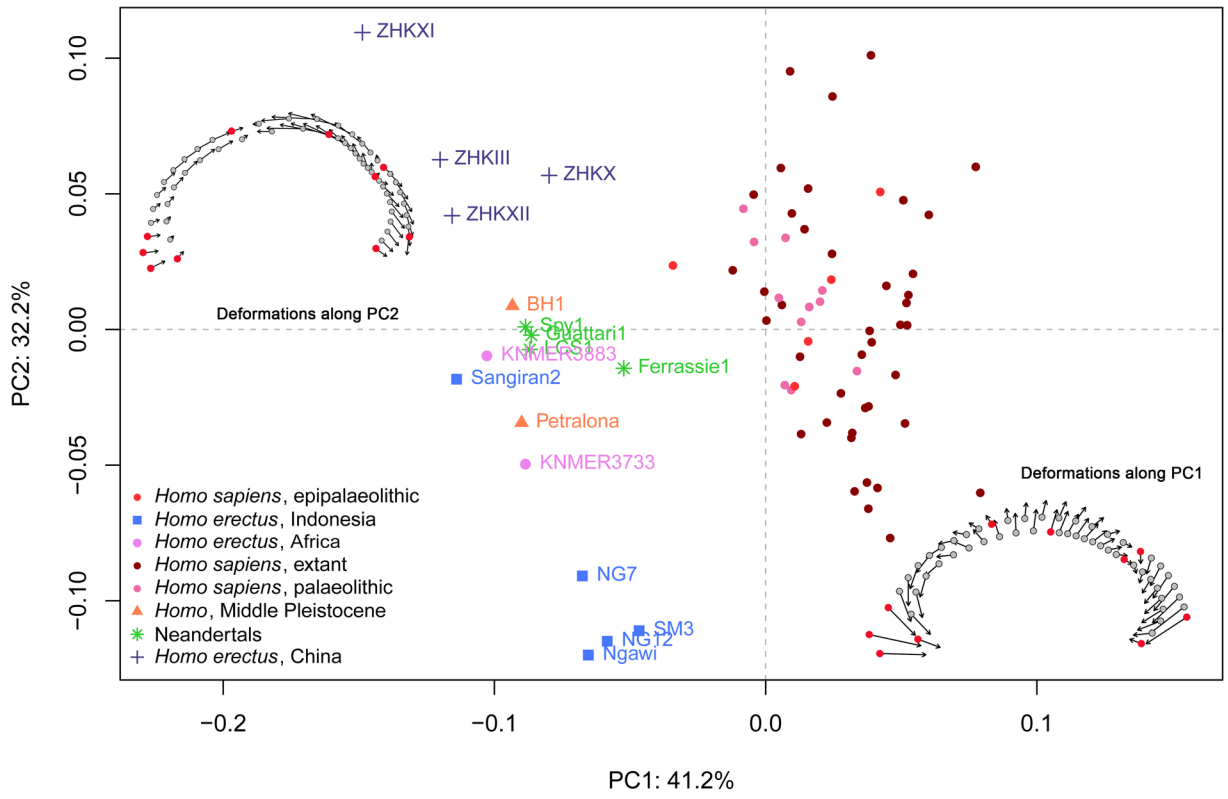

Figure 13. First and second principal components of the two-dimensional geometric morphometrics analysis of the exo and endocranial vaults in the skull's mid-sagittal plane for the complete sample of hominins and Homo sapiens *(n=73). Visualization of shape change along axes 1 and 2: circles=minimum conformation, arrowtips= maximum conformation, red points=fixed landmarks.*

The analysis of the fossil taxa only (Figure 14) shows a similar distribution of the specimens into clusters, but demonstrates a clearer separation between Neandertals and the rest of the middle cluster. Separation according to taxonomic, chronological, and geographical factors occurs along the axis of the PC1, which alone accounts for 68% of the total sample variation. The main shape variations represented are differences in the relative extension of the frontal and the parietal lobes and bones, and a thicker occipital torus in the specimens scoring positive numbers (in particular, the younger Indonesian *H. erectus* of Ngandong, Ngawi, and Sambungmacan). This thicker occipital torus is caused by an extension of the cranial vault, but also by an important reduction in the projection of the occipital lobe.

It is perhaps interesting to note that, in this analysis, Petralona and BH1, sometimes deemed to exhibit a shared suite of 'middle Pleistocene' characteristics, are found in diagonally opposed quadrants of the graph, although the distance between them is not greater than that between the most extreme Neandertals or the African *H. erectus* specimens.

DISCUSSION

BROKEN HILL 1 WITHIN THE HUMAN FOSSIL RECORD

We have detailed numerous internal features of BH1 (see also in Supplementary Information–SI1[2]) and have evaluated these traits relative to the available knowledge of other fossil hominins and extant hominids. Here, we synthesize and contextualize this new information.

The thick frontal torus and the distribution of CVT on the parietal bone distinguish BH1 (along with Petralona and Asian *H. erectus*; Balzeau 2013; Balzeau and Charlier 2016) from Neandertals and *H. sapiens* (Schwartz and Tattersall 2010). BH1 also shows a frontal keel that is not related to a clear variation in bone thickness. Indeed, it is only a slight relief on the external cranial surface compared to the variation in bone thickness due to wider endocranial traits. The bregmatic eminence on BH1 is related to a slight increase in the total bone thickness. These exocranial features have some variation in shape among *H. heidelbergensis* and *H. erectus* (e.g., Bräuer and Mbua 1992; Wu and Athreya 2013) and are not always related to a variation in CVT, because any extra thickness produced may be equalled or surpassed by variation in the shape of the bones or the presence of endocranial convolutions (Balzeau 2013). A relatively thick upper vault with relief on the exocranial surface, and on the endocranial surface, resulting in a thickening of the bone compared to the adjacent areas, was observed in *Pan paniscus* and Asian *H. erectus*. In these cases, bone thickness distribution resembles a cross radiating from the bregmatic area. We hypothesized that this "cross" pattern corresponds to the symplesiomorphic state

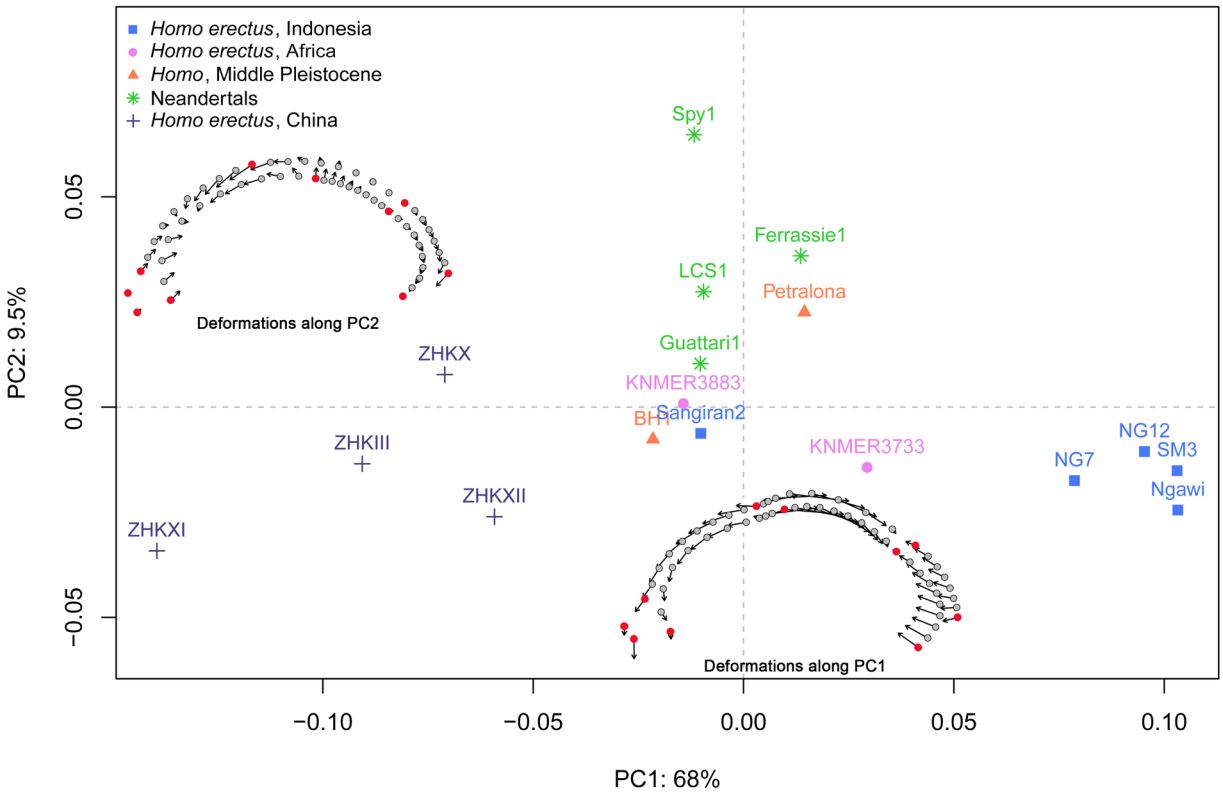

Figure 14. First and second principal components of the two-dimensional geometric morphometrics analysis of the exo and endocranial vaults in the skull's mid-sagittal plane for the fossil hominins (n=17). Visualization of shape change along axes 1 and 2: circles=minimum conformation, arrowtips= maximum conformation, red points=fixed landmarks.

among hominids (Balzeau 2013). In BH1, the sutures result in a reduced thickness along their course, but the general pattern resembles the plesiomorphic condition described above. Its degree of expression depends on the integration of many features: the external relief features, of course, but also the shapes of the bones and of the upper part of the frontal lobes. BH1 is robust when its superstructures are considered, and its high vault thickness is associated with a relatively large cranial size compared to other hominins. This combination is distinct in BH1, compared to the rest of the fossil hominin record, but BH1 does not display any of the apomorphic traits for CVT observed in either Neandertals or *H. sapiens*. This may be of interest in terms of the debate over whether it belongs to the species (often called *H. heidelbergensis*) that may represent the last common ancestor of these taxa. We need more detailed CVT data on mid-Pleistocene hominins to better appreciate the characteristics of BH1 and to identify possibly shared features that will help to recognize and define *H. rhodesiensis*/*H. heidelbergensis*.

Our study provides additional data to analyze and understand cranial features and their related internal variations that have been suggested to be diagnostic of the "mid-Pleistocene assemblage" (Rightmire 2001, 2004, 2013), including a lambda-inion chord (LIC) that exceeds the nuchal plane in length (IOC). This relationship, however, is not so simple. Indeed, only 14 of the 24 specimens attributed to *H. erectus* have LIC>IOC (Rightmire 2013). In addition, both BH1 and Petralona have a lower LIC/IOC ratio than several specimens attributed to *H. erectus* (Balzeau et al. 2011). There is a common organization of the occipital bone in the mid-sagittal plane shared by *H. erectus* and other robust hominin specimens, such as BH1, that distinguishes them from *H. sapiens*. As a result, exo- and endocranial proportions of the occipital bone as expressed by the LIC, IOC, L-endinion cord (LEC) and endinion-opisthion cord (EOC), the relative position of inion and endinion (Balzeau 2013), and the probable important thickness of the occipital torus—not preserved in BH1—support the view that BH1 resembles *H. erectus* in the morphology and dimensions of the occipital bone (Santa Luca 1978). In addition, Neandertals and *H. sapiens* have their own diagnostic morphology for this anatomical area. Neandertals show, among other features, a lambdoidal flattening, an occipital "bun," a weak and bilaterally arched occipital torus, and the presence of a suprainiac fossa (e.g., Balzeau and Rougier 2010). *H. sapiens* is characterized by a narrow and high occipital plane (Schwartz and Tattersall 2010).

The increase in vertex height that is proposed as characteristic of mid-Pleistocene hominins (Rightmire 2013) appears to be an allometric effect. Indeed, based on the data provided by Rightmire (2013), the ratio between the length of the skull (glabella-opisthocranion, GOL) and its height (porion-vertex, PVH) in BH1 (49.3) falls within the range

of variation of his sample of *H. erectus* (mean=51.6, SD=2.4). Similarly, the ratio of maximum endocranial height/maximum endocranial length in BH1 (70.2) is well within the variation observed for *H. erectus* and below the mean value for *H. sapiens* (Grimaud-Hervé 1997). As a result, the brain of BH1 is not relatively high compared to earlier hominins, and does not show the derived condition observed in later species.

The analysis of the profile morphology re-assesses the distance between the morphology of the *H. sapiens* skull and that of other *Homo* specimens. There is a complete separation between the fossils and the *H. sapiens* sample, and BH1 falls well within the fossil sample variation, showing no particular affinities to *H. sapiens*. This is due to the elongated profile and robust superstructures of BH1. When considered against the rest of the fossil sample, its position in the middle cluster is explained by the fact that the BH1 skull and endocast are robust, but do not show the reduced projection of the occipital area or the shorter frontal areas compared to the parietals that are seen in the Ngandong, Ngawi, and Sambungmacan individuals. On the PCA of the fossils (see Figure 14), PC1 (68% of sample variation) separates three clusters while PC2 (which accounts for a much smaller 9.5% of variation) separates Neandertals and the Petralona skull from most of the rest of the sample (*Homo erectus* and BH1). The position of BH1 on the plot suggests that it shows none of the strong characteristics exhibited by either the Zhoukoudian group (more gracile, with longer parietal areas compared with the frontal bones and lobes, and with a strongly projected occipital area on the endocranium) or the Ngandong/Ngawi/Sambungmacan group (thick tori, a less projected occipital region on the endocranium, and a longer frontal area relative to the parietal). BH1, unlike Petralona, does not appear to show any of the Neandertal characteristics either (retreating encephalic rostrum, a slightly shorter frontal area relative to the total length of the skull and endocast, and slightly elevated parietal lobes), or, if it does, they are not strongly expressed.

These results emphasize the ambiguous position of BH1 within the fossil record and do not allow us to either reject or accept close ties with putative *H. heidelbergensis* specimen Petralona. They do not suggest the shared characteristics with both Neandertals and *H. sapiens* that would be expected for a common ancestor either. Finally, the BH1 cranium and endocast do not show any strongly expressed exclusive diagnostic characteristics. In sum, concerning the cranial and endocranial profile of BH1, compared to other fossils, it does not allow us to clarify relationships between BH1 and its potential conspecifics or descendants, re-asserting instead that great caution should be exercised in the interpretation of this fossil until more specimens are known and available for analysis.

Le Cabec et al. (2013) suggest that the large dimensions of the roots of the anterior teeth in Neandertals could be an ancestral condition, also shared with early modern humans. This characteristic could contrast with the derived condition of more recent modern humans, which have reduced dimensions of their anterior teeth. The large sizes of the roots of the anterior teeth of BH1 are consistent with these observations and can be considered as an ancestral condition.

It has been suggested that enlarged paranasal sinus morphology is diagnostic of the *H. heidelbergensis* hypodigm (Prossinger et al. 2003; Seidler et al. 1997; Stringer 2012a). It seems that at least the frontal sinus may be distinctively large in this group compared to Neandertals and *H. sapiens* (Buck 2014; Prossinger et al. 2003; Seidler et al. 1997; Stringer 2012a; Zollikofer et al. 2008), while there is no difference in frontal sinus size between these latter taxa if cranial size is taken into account (Buck 2014; Rae et al. 2011; Zollikofer et al. 2008). The use of sinus size as a diagnostic trait for the hypodigm, however, is complicated by the variation that appears to be present in this trait in other taxa, such as *H. sapiens* (Brothwell et al. 1968; Buck 2014; Buckland-Wright 1970; Fernandez 2004a, b; Holton et al. 2013). Putative *H. heidelbergensis* also appear to display variation in sinus size; although Petralona, Bodo, and BH1 have all previously been noted to have large frontal sinuses (Prossinger et al. 2003; Seidler et al. 1997; Zollikofer et al. 2008), other specimens, such as Ceprano (Bruner and Manzi 2005) and Arago 21 (Balzeau 2005; Stringer 1984; Tillier 1975, 1977), appear to have small frontal sinuses.

Despite their consistently large, and possibly distinctive, paranasal sinus size, the *H. heidelbergensis* sample investigated here is not homogeneous. There are differences in relative volume between BH1, Bodo, and Petralona. These differences are not geographically patterned; there is as great a difference between Petralona (Europe) and Bodo (Africa) as between Bodo and BH1 (Africa), in terms of sinus volume. Moreover, both the putative *H. heidelbergensis* with small sinuses (Ceprano and Arago 21) and that with the largest frontal sinus (Petralona) are from Europe. The paranasal sinus evidence to date does not support a split between the African material and the European material, but could be argued to support the Euro-African hypodigm (see above). The problem of characterizing the level of *H. heidelbergensis* paranasal pneumatization can only be resolved with a larger sample of mid-Pleistocene fossils of different species.

The results reported here also suggest that the paranasal sinuses of BH1 may be particularly complex, but this could be due to the greater resolution of the BH1 microCT data. The other two fossils would need to be imaged comparably to make this statement with confidence. If this impression is borne out by data with improved resolution, however, it could have interesting implications in terms of sinus function theories. The majority of research to date supports the idea that the sinuses are spandrels, whose size largely depends on the size and shape of the bones they pneumatize (e.g., Buck 2014; Rae et al. 2011; Zollikofer et al. 2008). However, there also seems to be a large degree of variation not accounted for by this relationship, some of which may be due to exapted optimization for other purposes, for example, nitric oxide production (Lundberg 2008) or heat dumping during intense physical activity (Dean 1988; Churchill

2015; Irmak 2004). The greater area of highly vascularised epithelium available in a more complex sinus could be beneficial in either scenario. It is difficult to see why BH1 might require more nitric oxide or greater heat dumping capacity than its probable conspecifics, however, and in this case the variation is perhaps most likely to be stochastic.

BH1 shows a pattern of temporal bone pneumatization that is frequently seen in the genus *Homo*, with a well-pneumatized petromastoid area. Among fossil hominins, this pneumatization tends to be more reduced in specimens with larger brain size and with more vertical orientation of the lateral walls of the vault, compared to others with the opposite condition for these features. These latter features, together with an arched squamous temporal (e.g., Rightmire 2013), are said to be characteristics of middle Pleistocene hominins relative to *H. erectus*. Several additional specimens (e.g., Dali and Jinniushian) would be valuable in determining variation in temporal bone pneumatization in mid-Pleistocene hominins, and its interest for taxonomic attribution. Moreover, these additional analyses would also contribute to the ongoing debate on the developmental and/or functional origin of this pneumatization (Witmer 1997; Zollikofer and Weissmann 2008), as well as regarding the integration of this feature with the exocranial anatomy of the temporal bone.

Finally, the study of BH1 shows that this relatively large endocast is long and low. Globally, the morphometric analyses further illustrate that its shape does not display the specific features of either Neandertals or *H. sapiens*. Its pattern of endocast asymmetry is within the range of variation observed among other fossil hominins (Balzeau et al. 2012, 2014), but individual values for BH1 are small. However, endocranial features are well individualized. For example, the encephalic rostrum is short and large, the foot of the second parietal convolution is circular in shape and well individualized and the supramarginal gyrus is pronounced, meaning that the endocast, seen in posterior view, has lateral walls that are weakly convergent toward the top. These endocranial features are different from the condition observed in *H. erectus* but do not reach the degree of expression observed in Neandertals or modern humans.

PERSPECTIVES IN PALAEOANTHROPOLOGY

Throughout this paper, we have given precise descriptions of many internal anatomical features of Broken Hill 1, discovered nearly a century ago. Instead of doing separate analyses for each feature on restricted and unsatisfactory samples, we decided to focus here on all these anatomical aspects for the specimen. The information detailed here will be useful for future research, by us and others, and we hope that this work will stimulate similar exhaustive descriptions of other important fossil hominin specimens. Indeed, one dramatic limitation to this study has been the non-availability of appropriate comparative samples, since the anatomy for most of the features studied here has not yet been described for most of the other emblematic specimens from the mid-Pleistocene. This raises important issues for paleoanthropology. The recent announcement of *H. naledi* has been a topic of much discussion. However, one innovation of the scientists in charge of this collection has been to offer unfettered access to virtual models of most of the important specimens discovered (Berger et al. 2015).

In the future, we hope that this behavior will appear as the rule for publication of significant fossil hominins, instead of an exception. The paleoanthropological literature is full of papers describing fossils with few or no images in the classical orientations, with biplots obtained from geometric morphometric analyses that are impossible to reproduce, and with few meaningful measurements or coordinates that permit inclusion of the specimens in future studies. Scientific papers dealing with the anatomical description of hominin specimens, both in the case of announcement of new discoveries or for important specimens found many decades previously, should now always include qualitative and quantitative data that allow further independent research on the material.

CONCLUSION

CT or microCT data are useful tools to identify anatomical features, revealing internal and hidden characteristics. Moreover, detailed descriptions of key fossil hominins are important for potential interpretation of their anatomical features, as well as in the context of comparative studies. In the case of Broken Hill 1 we have tried to complete two important objectives. We give a detailed description of this specimen, including some anatomical aspects that had not been addressed before, and compare these with all the available information published for relevant fossil hominins.

Broken Hill 1 shows some unusual anatomical features, such as very extensive frontal paranasal pneumatization (in common with other potential *H. heidelbergensis*) and thick cranial bone. For many of the features analyzed, however, this fossil does not exhibit the apomorphic conditions observed in either Neandertals or among *H. sapiens*. The global shape of the brain and of the skull, including several features suggested to be diagnostic of the "mid-Pleistocene assemblage" (Rightmire 2001, 2004, 2013), may be partly explained by an allometric relationship relative to the features observed in *H. erectus s.l.* Moreover, no unique internal cranial features can be identified for this specimen.

These observations are important because a large part of the European hominin record—with the most notable exception of Petralona—that is approximately contemporary with BH1 shows some Neandertal affinities as conceptualized by the accretion model (e.g, Hublin 2009). The still unsettled question of the age of BH1 is important in this context. But complete description of other key fossil hominins and of their internal cranial features will be necessary before being able to discuss further the status, the definition and the geographic extension of *H. heidelbergensis* and/or *H. rhodesiensis*. Of course, one factor that complicates the discussion of this topic is that the holotype of *H. heidelbergensis* is a mandible and the available comparative material is very scarce, particularly outside Europe. Another limiting factor is the lack of high quality data available for many

relevant fossils; it is hoped that such information will soon be widely available for Petralona, Arago, Dali, Jinniushan, and the Sima de los Huesos sample, among many others, to help clarify the alpha taxonomy and phyletic position of these important mid-Pleistocene specimens.

ACKNOWLEDGMENTS

We are grateful to Robert Kruszynski for access to the Broken Hill 1 fossil and to Dan Sykes, Rebecca Summerfield and Farah Ahmed (all Natural History Museum, London) for access to the microCT scanner and the BH1 fossil. LTB thanks Ann MacLarnon for supervision, help and advice with her PhD, from which some of this paper is derived, and Gerhard Weber (University of Vienna) and George Koufos (Aristotle University of Thessaloniki) for access to Petralona CT data (Bodo CT data were purchased from the Digital Archives of Fossil Hominoids, University of Vienna). CBS and LTB thank the Calleva Foundation and the Human Origins Research Fund for funding. We thank the AST-RX platform (Accès Scientifique à la Tomographie à Rayons X), UMS 2700 « Outils et méthodes de la systématique intégrative », CNRS-MNHN, Paris, France, for the micro-CT scanning procedures on the specimen housed in Paris. AB is grateful to Aurélie Fort, Véronique Laborde, and Miguel Garcia-Sanz for technic and scientific assistance during the realization of the research at the MNHN. This work benefited from discussion with G. Clément.

ENDNOTE

1. It should be noted that some of the authors prefer the spelling "Neanderthal."
2. Supplementary Information-SI1: complete landmark description of the skull including definition of the landmarks and their coordinates.

REFERENCES

Adams, D.C. and Otarola-Castillo E. 2013. geomorph: an R package for the collection and analysis of geometric morphometric shape data. *Methods in Ecology and Evolution* 4, 393–399.

Albessard, L., Grimaud-Hervé, D., and Balzeau A. 2016. Evolution of cranial and endocranial profiles in *Homo* species. A study in 2D geometric morphometrics. *BMSAP* 28, 118–131.

Allam, A.F. 1969. Pneumatization of the temporal bone. *Annals of Otology, Rhinology, and Laryngology* 78, 49–64.

Antón, S.C. 1997. Developmental age and taxonomic affinity of the Mojokerto child, Java, Indonesia. *American Journal of Physical Anthropology* 102, 497–514.

Baba, H., Aziz, F., Kaifu, Y., Suwa, G., Kono, R.T., and Jacob, T. 2003. *Homo erectus* calvarium from the Pleistocene of Java. *Science* 299, 1384–1388.

Balzeau, A. 2005. *Spécificités des caractères morphologiques internes du squelette céphalique chez Homo erectus*. Ph.D. Dissertation, Muséum national d'histoire naturelle, Paris.

Balzeau, A. 2006. Are thickened cranial bones and equal participation of the three structural bone layers autapomorphic traits of *Homo erectus*? *Bulletin et Mémoires de la Societé d'Anthropologie de Paris* 18, 145–163.

Balzeau A. and Grimaud-Hervé D. 2006. Cranial base morphology and temporal bone pneumatization in Asian *Homo erectus*. *Journal of Human Evolution* 51, 350–359.

Balzeau, A. 2007. Variation and characteristics of the cranial vault thickness in Krapina and Western European Neandertals. *Periodicum Biologorum* 109, 369–377.

Balzeau, A. 2015. Comparative aspects of temporal bone pneumatisation in some African fossil hominins. *BMSAP* 27, 135–141.

Balzeau, A. and Radovčić, J. 2008. Variation and modalities of growth and development of the temporal bone pneumatization in Neandertals. *Journal of Human Evolution* 54, 546–567.

Balzeau, A., Crevecoeur, I., Rougier, H., Froment, A., Gilissen, E., Grimaud-Hervé, D., Mennecier, P., and Semal, P. 2010. Applications of imaging methodologies to paleoanthropology: beneficial results relating to the preservation, management and development of collections. *Comptes Rendus Palevol* 9, 265–275.

Balzeau, A. and Rougier, H. 2010. Is the suprainiac fossa a Neandertal autapomorphy? A complementary external and internal investigation. *Journal of Human Evolution* 58, 1–22.

Balzeau A. and Gilissen E. 2010. Endocranial shape asymmetries in *Pan paniscus*, *Pan troglodytes* and *Gorilla gorilla* assessed via skull based landmark analysis. *Journal of Human Evolution* 59, 54–69.

Balzeau, A., Grimaud-Hervé, D., and Gilissen, E. 2011. Where are inion and endinion? Variations of the exo- and endocranial morphology of the occipital bone during hominin evolution. *Journal of Human Evolution* 61, 488–502.

Balzeau, A., Holloway, R.L., and Grimaud-Hervé, D. 2012. Variations and asymmetries in regional brain surface in the genus *Homo*. *Journal of Human Evolution* 62, 696–706.

Balzeau, A., Grimaud-Hervé, D., Détroit, F., Holloway, R.L., Combès, B., and Prima, S. 2013. First description of the Cro-Magnon 1 endocast and study of brain variation and evolution in anatomically modern *Homo sapiens*. *Bulletin et Mémoires de la Societé d'Anthropologie de Paris* 25, 1–18.

Balzeau, A. 2013. Thickened cranial vault and parasagittal keeling, correlated traits and autapomorphies of *Homo erectus*? *Journal of Human Evolution* 64, 631–644.

Balzeau, A., Gilissen, E., Holloway, R.L., Prima, S., and Grimaud-Hervé, D. 2014. Variations in size, shape and asymmetries of the third frontal convolution in hominids: paleoneurological implications for hominin evolution and the origin of language. *Journal of Human Evolution* 76, 116–128.

Balzeau, A. and Charlier P. 2016. What do cranial bones of LB1 tell us about *Homo floresiensis*? *Journal of Human Evolution* 93, 12–24.

Bartsiokas, A. and Day, M.H. 1993. Lead poisoning and dental caries in the Broken Hill hominid. *Journal of Human Evolution* 24, 243–249.

Berger, L.R., Hawks, J., de Ruiter, D.J., Churchill, S.E.,

Schmid, P., Delezene, L.K., Kivell, T.L., Garvin, H.M., Williams, S.A., DeSilva, J.M., Skinner, M.M., Musiba, C.M., Cameron, N., Holliday, T.W., Harcourt-Smith, W., Ackermann, R.R., Bastir, M., Bogin, B., Bolter, D., Brophy, J., Cofran, Z.D., Congdon, K.A., Deane, A.S., Dembo, M., Drapeau, M., Elliott, M.C., Feuerriegel, E.M., Garcia-Martinez, D., Green, D.J., Gurtov, A., Irish, J.D., Kruger, A., Laird, M.F., Marchi, D., Meyer, M.R., Nalla, S., Negash, E.W., Orr, C.M., Radovcic, D., Schroeder, L., Scott, J.E., Throckmorton, Z., Tocheri, M.W., VanSickle, C., Walker, C.S., Wei, P., and Zipfel, B. 2015. *Homo naledi*, a new species of the genus *Homo* from the Dinaledi Chamber, South Africa. *eLife* 2015;4: e09560.

Blake, C.C. 1864. On the alleged peculiar characters, and assumed antiquity of the human cranium from the Neanderthal. *Journal of the Anthropological Society of London* 2, cxxxix-clvii.

Blaney, S.P.A. 1990. Why paranasal sinuses? *Journal of Laryngology and Otology* 104, 690–693.

Brace, C.L. 1962. Cultural factors in the evolution of the human dentition. In: Montagu, M.F.A. (ed.), *Culture and the Evolution of Man*. Oxford University Press, New York, pp. 343–354.

Brace, C.L. 1975. Comment on 'Did La Ferrassie I use his teeth as tools? *Current Anthropology* 16, 396–397.

Bräuer, G. 1990. The occurrence of some controversial *Homo erectus* cranial features in the Zhoukoudian and East African hominids. *Acta Anthropologica Sinica* 9, 350–358.

Bräuer, G. and Mbua, E. 1992. *Homo erectus* features used in cladistics and their variability in Asian and African hominids. *Journal of Human Evolution* 22, 79–108.

Bronoosh, P., Shakibafard, A., Mokhtare, M.R., and Munesi Rad, T. 2014. Temporal bone pneumatization: a computed tomography study of pneumatized articular tubercule. *Clinical Radiology* 69, 151–156.

Brothwell, D.R., Molleson, T., and Metreweli, C. 1968. Radiological aspects of normal variation in earlier skeletons: an exploratory study. In: Brothwell, D.R. (ed.), *The Skeletal Biology of Earlier Populations*. Pergammon Press, Oxford, pp. 149–172.

Brown, P. 1994. Cranial vault thickness in Asian *Homo erectus* and *Homo sapiens*. *Courier Forschungsinstitut Senckenberg* 171, 33–46.

Bruner, E. and Manzi, G. 2005. CT-based description and phyletic evaluation of the archic human calvarium from Ceprano, Italy. *Anatomical Record* 285A, 643–658.

Buck, L.T., Stringer, C.B., MacLarnon, A.M., and Rae, T.C. 2012. Paranasal sinus shape in Pleistocene hominins. *American Journal of Physical Anthropology* 147, 108.

Buck, L.T. 2014. *Craniofacial Morphology, Adaptation and Paranasal Pneumatisation in Late Pleistocene Hominins*. Ph.D. Thesis, University of Roehampton, London.

Buck, L.T. and Stringer, C.B. 2014. *Homo heidelbergensis*. *Current Biology* 24, R214–215.

Buck, L.T. and Stringer, C.B. 2015. A rich locality in South Kensington: The fossil hominin collection of the Natural History Museum, London. *Geological Journal* 50, 321–337.

Buckland-Wright, J.C. 1970. A radiographic examination of frontal sinuses in early British populations. *Man* 5, 512–517.

Busk, G. 1861. Translation with comments of "On the crania of the most ancient races of man" by D. Schaafhausen. *Natural History Review* April 1861, 155–175.

Butaric, L.N., McCarthy, R.C., and Broadfield, D.C. 2010. A preliminary 3D computed tomography study of the human maxillary sinus and nasal cavity. *American Journal of Physical Anthropology* 143, 426–436.

Churchill, S.E. 1998. Cold adaptation, heterochrony and Neandertals. *Evolutionary Anthropology* 7, 46–60.

Churchill, S.E. 2015. *Thin on the Ground: Neandertal Biology, Archeology & Ecology*. Wiley Blackwell, Hoboken, NJ.

Clark, J.D., de Heizelin, J., Schick, K., Hart, W.K., White, T.D., WoldeGabriel, G., Walter, R. C., Suwa, W., Asfaw, B., Vrba, E., and Selassie, Y.H., 1994. African *Homo erectus*: old radiometric ages and young Oldowan assemblages in the Middle Awash Valley, Ethiopia. *Science* 264, 1907–1910.

Copes, L. 2012. *Comparative and Experimental Investigations of Cranial Robusticity in Mid-Pleistocene Hominins*. Ph.D. dissertation, Arizona State University, Tempe, USA.

Crawford, J.R. and Howell, D.C. 1998. Comparing an individual's test score against norms derived from small samples. *The Clinical Neuropsychologist* 12, 482–486.

Curnoe, D. and Brink, J. 2010. Evidence of pathological conditions in the Florisbad cranium. *Journal of Human Evolution* 59, 504–513.

Curnoe, D. and Green, H. 2013. Vault thickness in two Pleistocene Australian crania. *Journal of Archaeological Science* 40, 1310–1318.

Dean, M.C. 1988. Another look at the nose and the functional significance of the face and nasal mucous-membrane for cooling the brain in fossil hominids. *Journal of Human Evolution* 17, 715–718.

Delson, E., Harvati, K., Reddy, D., Marcus, L.F., Mowbray, K., Sawyer, G.J., Jacob, T., and Márquez, S. 2001. The Sambungmacan 3 calvaria: a comparative morphometric and morphological analysis. *Anatomical Record* 262, 380–397.

Dryden, I.L. 2013. Shapes: statistical shape analysis. R Package version 1.1-8." http://cran.r-project.org/package=shapes

Elliot Smith, G. 1928. Endocranial cast obtained from the Rhodesian skull. In: Pycraft, W.P., (ed.) *Rhodesian Man and Associated Remain*. British Museum (Natural History), London.

Farke, A.A. 2010. Evolution and functional morphology of the frontal sinuses in Bovidae (Mammalia: Artiodactyla), and implications for the evolution of cranial pneumaticity. *Zoological Journal of the Linnean Society* 159, 988–1014.

Fernandez, C.L. 2004a. Forensic ethnic identification of crania: the role of the maxillary sinus—a new approach. *American Journal of Forensic Medicine and Pathology* 25, 302–313.

Fernandez, C.L. 2004b. Volumetric analysis of maxillary sinuses of Zulu and European crania by helical, multislice computed tomography. *Journal of Laryngology and Otology* 118, 877–881.

Galaburda, A.M., LeMay, M., Kemper, T.L., and Geschwind, N. 1978. Right-left asymmetries in the brain. *Science* 199, 852–856.

Gauld, S.C. 1996. Allometric patterns of cranial bone thickness in fossil hominids. *American Journal of Physical Anthropology* 100, 411–426.

Grimaud-Hervé, D. 1997. *L'Évolution de l'Encéphale chez Homo erectus et Homo sapiens: Exemples de l'Asie et de l'Europe*. Cahiers de Paléoanthropologie. CNRS, Paris.

Grimaud-Hervé, D. and Lordkipanidze, D. 2010. The fossil hominid's brain of Dmanisi: D 2280 and D 2282. In Yuan, M.S. and Broadfield, D.C. (eds.), *The Human Brain Evolving: A Symposium in Honor of Professor Ralph L. Holloway*, Indiana University, Bloomington, pp. 60–82.

Grimaud-Hervé, D., Widianto, H., Détroit, F., and Sémah, F. 2012. Comparative morphological and morphometric description of the hominin calvaria from Bukuran (Sangiran, central Java, Indonesia). *Journal of Human Evolution* 63, 637–652.

Grün, R. 1996. A re-analysis of electron spin resonance dating results associated with the Petralona hominid. *Journal of Human Evolution* 30, 227–241.

Hammer, O., Harper, D.A.T., and Ryan, P.D. 2001. PAST: Palaeontological Statistics software package for education and data analysis. *Palaeontologia Electronica* 4(1), 9 pp.

Harvati, K. 2007. 100 years of *Homo heidelbergensis* - life and times of a controversial taxon. *Mitteilungen der Gesellschaft für Urgeschichte* 16, 85–94.

Hill, C.A. 2008. *Evolutionary and Developmental History of Temporal Bone Pneumatization in Hominids*. Ph.D. Dissertation, Pennsylvania State University, Pittsburgh, USA.

Hill, C.A. and Richtsmeier, J.T. 2008. A quantitative method for the evaluation of three-dimensional structure of temporal bone pneumatization. *Journal of Human Evolution* 55, 682–690.

Hill, C.A. 2011. Ontogenetic changes in temporal bone pneumatization in humans. *Anatomical Record* 7, 1103–1115.

Holloway, R.L., Broadfield, D.C., and Yuan, M.S. 2004. The human fossil record. In: Holloway, R., Broadfield, D.C., Yuan, M.S., Schwartz, J.H., and Tattersall, I. (eds.), *The Human Fossil Record. Brain Endocasts: The Paleoneurological Evidence*, volume 3. Wiley-Liss, Hoboken, NJ.

Holton, N., Yokley, T., and Butaric, L. 2013. The morphological interaction between the nasal cavity and maxillary sinuses in living humans. *Anatomical Record* 296, 414–426.

Hublin, J.J. 1978. *Le torus occipital transverse et les structures associées: évolution dans le genre Homo*. Ph.D. Dissertation, Université Paris VI, Paris, France.

Hublin, J.J. 2009. The origin of Neandertals. *Proceedings of the National Academy of Sciences USA* 106, 16022–16027.

Indriati, E. and Antón, S.C. 2010. The calvaria of Sangiran 38, Sendangbusik, Sangiran Dome, Java. *Homo* 61, 225–243.

Irmak, M.K., Korkmaz, A., and Erogul, O. 2004. Selective brain cooling seems to be a mechanism leading to human craniofacial diversity observed in different geographical regions. *Medical Hypotheses* 63, 974–979.

Kappelman, J., Alçiçek, M.C., Kazanci, N., Schultz, M., Özkul, M., and Şen, Ş. 2008. First *Homo erectus* from Turkey and implications for migrations into temperate Eurasia. *American Journal of Physical Anthropology* 135, 110–116.

Kennedy, G.E. 1991. On the autapomorphic traits of *Homo erectus*. *Journal of Human Evolution* 20, 375–412.

Kennedy, K.A.R., Sonakia, A., Chiment, J., and Verma, K.K. 1991. Is the Narmada hominid an Indian *Homo erectus*? *American Journal of Physical Anthropology* 86, 475–496.

Kertesz, A., Polk, M., Black, S.E., and Howell, J. 1990. Sex, handedness, and the morphometry of cerebral asymmetries on magnetic resonance imaging. *Brain Research* 530, 40–48.

Klein, R.G. 1973. Geological antiquity of Rhodesian Man. *Nature*, 244, 311–312.

Klein, R.G. 2009. *The Human Career: Human Biological and Cultural Origins*. University of Chicago Press, Chicago.

Koppe, T., Nagai, H., and Rae, T.C. 1999a. Factors in the evolution of the primate paranasal sinuses. In: Koppe, T., Nagai, H., and Alt, K.W. (eds.), *The Paranasal Sinuses of Higher primates: Development, Function and Evolution*. Quintessence, Chicago, pp. 151–175.

Koppe, T., Rae, T.C., and Swindler, D.R. 1999b. Influence of craniofacial morphology on primate paranasal pneumatization. *Annals of Anatomy* 181, 77–80.

Lacy, S.A. 2014. The oral pathological conditions of the Broken Hill (Kabwe) 1 cranium. *International Journal of Paleopathology* 7, 57–63.

Le Cabec, A., Gunz, P., Kupczik, K., Braga, J., and Hublin, J.J. 2013. Anterior tooth root morphology and size in Neanderthals: taxonomic and functional implications. *Journal of Human Evolution* 64, 169–193.

Le Gros Clark, W.E. 1964. *The Fossil Evidence for Human Evolution: An Introduction to the Study of Paleoanthropology*, 2nd edition. University of Chicago Press, Chicago.

LeMay M. 1977. Asymmetries of the skull and handedness. *Journal of Neuroscience* 32, 243–253.

Lumley de, M.A., Gabounia, L, Vekua, A., and Lordkipanidze, D. 2006. Les restes humains du Pliocène final et du début du Pléistocène inférieur de Dmanissi, Géorgie (1991-2000). I – les crânes, D 2280, D2282, D 2700. *L'Anthropologie* 110, 1–110.

Lund, V.J. 1988. The maxillary sinus in the higher primates. *Acta Oto-Laryngologica* 105, 163–171.

Lundberg, J.O. 2008. Nitric oxide and the paranasal sinuses. *Anatomical Record* 291, 1479–1484.

Manzi, G. 2016. Humans of the Middle Pleistocene: the controversial calvarium from Ceprano (Italy) and its significance for the origin and variability of *Homo heidelbergensis*. *Quaternary International* 411, 254–261.

Manzi, G., Bruner, E., and Passarello, P. 2003. The one-

million-year-old *Homo* cranium from Bouri (Ethiopia): a reconsideration of its *H. erectus* affinities. *Journal of Human Evolution* 44, 731–736.

Marsh, H.E. 2013. *Beyond Thick versus Thin: Mapping Cranial Vault Thickness Patterns in Recent Homo sapiens*. Ph.D. dissertation, University of Iowa, Ames, USA.

Millard, A.R. 2008. A critique of the chronometric evidence for hominid fossils: I. Africa and the Near East 500-50 ka. *Journal of Human Evolution* 54, 848–874.

Moore, N.C., Skinner, M.M., and Hublin, J.J. 2013. Premolar root morphology and metric variation in *Pan troglodytes verus*. *American Journal of Physical Anthropology* 150, 632–646.

Moore, N.C., Hublin, J.J., and Skinner, M.M. 2015. Premolar root and canal variation in extant non-human hominoidea. *American Journal of Physical Anthropology* 158, 209–226.

Moss, M.L. and Young, R.W. 1960. Functional approach to craniology. *American Journal of Physical Anthropology* 18, 281–292.

Montgomery, P.Q., Williams, H.O.L., and Stringer, C.B. 1994. An assessment of the temporal bone lesions of the Broken Hill cranium. *Journal of Archaeological Science* 21, 331–337.

Mounier, A. 2009. *The Validity of the Taxon Homo heidelbergensis Schoetensack, 1908*. Ph.D. Thesis, Université de la Mediterranée, Marseille.

Mounier, A., Marchal, F., and Condemi, S. 2009. Is *Homo heidelbergensis* a distinct species? New insight on the Mauer mandible. *Journal of Human Evolution* 56, 219–246.

Oakley, K.P., Campbell, B.G., and Molleson, T.I. 1977. *Catalogue of Fossil Hominids. Part I: Africa*, Second edition. The Trustees of The British Museum (Natural History), London.

Palmer, A.R., 1994. Fluctuating asymmetry analyzes: a primer. In: Markow, T.A. (ed.), *Developmental Instability: Its Origins and Evolutionary Implications*. Kluwer Academic Publishers, Dordrecht, pp. 335–364.

Pope, G.G. 1992. Craniofacial evidence for the origin of modern humans in China. *Yearbook of Physical Anthropology* 35, 243–298.

Potts, R., Behrensmeyer, A.K., Deino, A., Ditchfield, P., and Clark, J. 2004. Small mid-Pleistocene hominin associated with East African Acheulean technology. *Science* 305, 75–78.

Prossinger, H., Seidler, H., Wicke, L., Weaver, D., Recheis, W., Stringer, C., and Müller, G. 2003. Electronic removal of encrustations inside the Steinheim cranium reveals paranasal sinus features and deformations, and provides a revised endocranial volume estimate. *Anatomical Record* 273B, 132–142.

Pycraft, W.P. 1928. *Rhodesian Man and Associated Remains*. British Museum (Natural History), London.

Rae, T.C. 1999. The maxillary sinus in primate paleontology and systematics. In: Koppe, T., Nagai, H., and Alt, K.W. (eds.), *The Paranasal Sinuses of Higher Primates.* Quintessence, Chicago, pp. 177-189.

Rae, T.C. and Koppe, T. 2000. Isometric scaling of maxillary sinus size in Hominoidea. *Journal of Human Evolution* 38, 411–423.

Rae, T.C., Koppe, T., and Stringer, C.B. 2011. The Neanderthal face is not cold adapted. *Journal of Human Evolution* 60, 234–239.

Rightmire, G.P. 1996. The human cranium from Bodo, Ethiopia: evidence for speciation in the middle Pleistocene? *Journal of Human Evolution* 31, 21–39.

Rightmire, G.P. 1998. Human evolution in the Middle Pleistocene: the role of *Homo heidelbergensis. Evolutionary Anthropology* 6, 218–227.

Rightmire, G.P. 2001. Patterns of hominid evolution and dispersal in the middle Pleistocene. *Quaternary International* 75, 77–84.

Rightmire, G.P. 2004. Brain size and encephalization in early to mid-pleistocene *Homo*. *American Journal of Physical Anthropology* 124, 109–123.

Rightmire, G.P., Lordkipanidze, D., and Vekua, A. 2006. Anatomical descriptions, comparative studies and evolutionary significance of the hominin skulls from Dmanisi, Republic of Georgia. *Journal of Human Evolution* 50, 115–141.

Rightmire, G.P. 2008. *Homo* in the middle Pleistocene: hypodigms, variation, and species recognition. *Evolutionary Anthropology* 17, 8–21.

Rightmire, G.P. 2013. *Homo erectus* and Middle hominins: brain size, skull form, and species recognition. *Journal of Human Evolution* 65**,** 223–252.

Rightmire, G.P. 2017. *Middle Pleistocene Homo Crania from Broken Hill and Petralona: Morphology, Metric Comparisons, and Evolutionary Relationships. In Human Paleontology and Prehistory*. Springer International Publishing, Dordrecht, pp. 145–159.

Rohlf, F.J. 2008. TpsRelw v1.46. Department of Ecology and Evolution, State University of New York. http://life.bio.sunysb.edu.morph/

Rohlf, F.J. 2009.TpsDig v2.14. Department of Ecology and Evolution, State University of New York. http://life.bio.sunysb.edu.morph/

Rosas, A., Peña, A., Garcia-Tabernero, A., Bastir, M., De la Rasilla, M., and Fortea, J. 2008. Endocranial occipitotemporal anatomy of the SD-1219 fossil from the El Sidrón Neandertals. *Anatomical Record* 291, 502–512.

Santa Luca, A.P. 1978. A re-examination of presumed Neandertal-like fossils. *Journal of Human Evolution* 7, 619–636.

Scheuer, L. and Black, S. 2000. *Developmental Juvenile Osteology*. Academic Press, San Diego, CA.

Schlager, S. 2013. Morpho: calculations and visualisations related to geometric morphometrics. R Package version 0.25-1. http://cran.r-project.org/package=Morpho

Schulter, F.P. 1976. A comparative study of the temporal bone in three populations of man. *American Journal of Physical Anthropology* 44, 453–468.

Schulter-Ellis, F.P. 1979. Population differences in cellularity of the mastoid process. *Acta Oto-Laryngologica* 87, 461–465.

Schwartz, J.H. and Tattersall, I. 2002. *The Human Fossil Record*. Volume Two. *Craniodental Morphology of Genus Homo (Africa and Asia)*. John Wiley and Sons, Inc., Publications, New York.

Schwartz, J.H. and Tattersall, I. 2010. Fossil evidence for the origin of *Homo sapiens*. *Yearbook of Physical Anthropology* 53, 94–121.

Schwartz, G.T., Thackeray, J.F., Reid, C., and Van Reenan, J.F. 1998. Enamel thickness and the topography of the enamel-dentine junction in South Africa Plio-Pleistocene hominids with special reference to the Carabelli trait. *Journal of Human Evolution* 35, 523–542.

Seidler, H., Falk, D., Stringer, C., Wilfing, H., Muller, G.B., zur Nedden, D., Weber, G.W., Reicheis, W., and Arsuaga, J.L. 1997. A comparative study of stereolithographically modelled skulls of Petralona and Broken Hill: implications for future studies of middle Pleistocene hominid evolution. *Journal of Human Evolution* 33, 691–703.

Shea, B.T. 1977. Eskimo craniofacial morphology, cold stress and maxillary sinus. *American Journal of Physical Anthropology* 47, 289–300.

Smith, F.H. 1976. On anterior tooth wear at Krapina and Ochoz. *Current Anthropology* 17, 167–168.

Smith, F.H. and Paquette, S.P. 1989. The adaptive basis of Neandertal facial form, with some thoughts on the nature of modern human origins. In: E. Trinkaus (ed.), *The Emergence of Modern Humans: Biocultural Adaptations in the Later Pleistocene*. Cambridge University Press, Cambridge, pp. 181–210.

Smith, T.M., Olejniczak, A.J., Zermeno, J.P., Tafforeau, P., Skinner, M.M., Hoffmann, A., Radovčić, J., Toussaint, M., Kruszynski, R., Menter, C., and Moggi-Cecchi, J. 2012. Variation in enamel thickness within the genus *Homo*. *Journal of Human Evolution* 62, 395–411.

Sokal, R.R. and Rohlf, J.F. 1995. *Biometry*. W.H. Freeman, San Francisco, CA.

Spoor, F. and Zonneveld, F. 1993. The bony labyrinth in *Homo erectus*: a preliminary report. *Courier Forschungsinstitut Senckenberg* 171, 251–256.

Spoor, F., Jeffery, N., and Zonneveld, F. 2000. Using diagnostic radiology in human evolutionary studies. *Journal of Anatomy* 197, 61–76.

Stringer, C.B. 1983. Some further notes on the morphology and dating of the Petralona hominid. *Journal of Human Evolution* 12, 731–742.

Stringer, C. 1984. The definition of *Homo erectus* and the existence of the species in Africa and Europe. *Courier Forschungsinstitut Senckenberg* 69, 131–144.

Stringer, C. 1985. Middle Pleistocene hominid variability and the origin of Late Pleistocene humans. In: Delson, E. (ed.) *Ancestors: The Hard Evidence.* Alan R. Liss, New York, pp. 289–295.

Stringer, C.B. 2002. Modern human origins: progress and prospects. *Philosophical Transactions of the Royal Society B* 357, 563–579.

Stringer, C. 2012a. The status of *Homo heidelbergensis* (Schoetensack 1908). *Evolutionary Anthropology* 21, 101–107.

Stringer, C. 2012b. Evolution: what makes a modern human. *Nature* 485, 33–35.

Stringer, C. 2013. *Lone Survivors*. Times Books, New York.

Stringer, C.B. and Buck, L.T. 2014. Diagnosing *Homo sapiens* in the fossil record. *Annals of Human Biology* 41, 312–322.

Tillier, A.M. 1975. *Les sinus craniens chez les hommes actuels et fossiles: essai d'interpretation*. Doctorat de 3eme Cycle. Univerisite de Paris VI, Paris.

Tillier, A.M. 1977. La pneumatisation du massif craniofacial chez les hommes actuels et fossiles. *Bulletin et Mémoires de la Societé d'Anthropologie de Paris* 4, XIII, 177–189.

Vinyard, C.J. and Smith, F.H. 1997. Morphometric relationships between the supraorbital region and frontal sinus in Melanesian crania. *Homo* 48, 1–21.

Virapongse, C., Sarwar, M., Bhimani, S., Sasaki, C., and Shapiro, R. 1985. Computed tomography of temporal bone pneumatization: 1. Normal pattern and morphology. *American Journal of Roentgenology* 147, 473–481.

Weidenreich, F. 1943. The skull of *Sinanthropus pekinensis*: a comparative study of a primitive hominid skull. *Palaeontologia Sinica* D10, 1–484.

Witmer, L.M. 1997. The evolution of the antorbital cavity of archosaurs: a study in soft-tissue reconstruction in the fossil record with an analysis of the function of pneumaticity. *Journal of Vertebrate Paleontology* 17, 1–74.

Wolfowitz, B.L. 1974. *Pneumatization of the Skull of the South African Negro*. Ph.D. Dissertation, University of the Witwatersrand, Johannesburg, South Africa.

Wood, B. 1984. The origin of *Homo erectus*. *Courier Forschungsinstitut Senckenberg* 69, 389–406.

Wood, B. (ed.) 2011. *Wiley-Blackwell Encyclopedia of Human Evolution*. Blackwell Publishing Ltd., Oxford.

Woodward, A.S. 1921. A new cave man from Rhodesia, South Africa. *Nature* 108, 371–372.

Wu, X. and Athreya, S. 2013. A description of the geological context, discrete traits, and linear morphometrics of the Middle Pleistocene hominin from Dali, Shaanxi Province, China. *American Journal of Physical Anthropology* 150, 141–157.

Zollikofer, C., Ponce de León, M., Schmitz, R., and Stringer, C. 2008. New insights into Mid-Late Pleistocene fossil hominin paranasal sinus morphology. *Anatomical Record* 291, 1506–1516.

Zollikofer, C.P.E. and Weissmann, J.D. 2008. A morphogenetic model of cranial pneumatization based on the invasive tissue hypothesis. *Anatomical Record* 11, 1446–1454.

Zonneveld, F. 1987. *Computed Tomography of the Temporal Bone and Orbit*. Urban & Schwarzenberg, Munich.